

## DEVELOPMENTAL BIOLOGY

# Deciphering epiblast lumenogenesis reveals proamniotic cavity control of embryo growth and patterning

Yung Su Kim<sup>1</sup>, Rui Fan<sup>1</sup>, Ludmila Kremer<sup>2</sup>, Nannette Kuempel-Rink<sup>2</sup>, Karina Mildner<sup>3</sup>, Dagmar Zeuschner<sup>3</sup>, Liesbeth Hekking<sup>4</sup>, Martin Stehling<sup>5</sup>, Ivan Bedzhov<sup>1\*</sup>

During the peri-implantation stages, the mouse embryo radically changes its appearance, transforming from a hollow-shaped blastocyst to an egg cylinder. At the same time, the epiblast gets reorganized from a simple ball of cells to a cup-shaped epithelial monolayer enclosing the proamniotic cavity. However, the cavity's function and mechanism of formation have so far been obscure. Through investigating the cavity formation, we found that in the epiblast, the process of lumenogenesis is driven by reorganization of intercellular adhesion, vectorial fluid transport, and mitotic paracellular water influx from the blastocoel into the emerging proamniotic cavity. By experimentally blocking lumenogenesis, we found that the proamniotic cavity functions as a hub for communication between the early lineages, enabling proper growth and patterning of the postimplantation embryo.

## INTRODUCTION

All tissues of the fetus originate from a small ball of pluripotent epiblast cells positioned inside the blastocyst. The epiblast lineage is established during the first days of embryonic development, as the result of two subsequent cell fate decisions, which also specify the early extraembryonic lineages, namely, the trophoctoderm (TE) and the primitive endoderm (PE). At embryonic day 4 and a half (E4.5), the mouse blastocyst attaches to the uterine wall and invades the maternal tissues. In turn, the uterine stroma rapidly proliferates, forming the decidua that completely engulfs and conceals the implanting embryo, hindering direct observations and experimental manipulations. In the next days, the blastocyst transforms into an early egg cylinder, where patterning and differentiation of the pluripotent lineage is initiated, setting up the blueprint of the future body (1).

During the peri-implantation stages, the epiblast undergoes extensive tissue-scale reorganization, transforming from a coherent ball of cells to a polarized epithelium. Polarization cues from the surrounding basement membrane (BM), transmitted via integrin receptors, direct the orientation of the apical-basal polarity axis in the epiblast. As a result of coordinated epithelialization, the apical domain is established de novo in the center of the epiblast (2, 3). This tissue-scale reorganization can be faithfully recapitulated in vitro by culturing embryonic stem cells (ESCs) in a three-dimensional (3D) hydrogel of extracellular matrix proteins (Matrigel) that mimic the BM function, providing an accessible in vitro model of epiblast morphogenesis (2, 3).

This transition from the pre- to postimplantation epiblast is also associated with the formation of the proamniotic cavity. Previous studies have suggested that the process of cavitation depends on

programmed cell death, which allows for the core of the epiblast to be carved out (4, 5). Yet, a more recent study has refuted this model, showing that the formation of the proamniotic cavity is independent of apoptosis but is instead associated with the reorganization of the epiblast into an epithelial rosette-like structure, where the central lumen emerges and expands (2). However, the mechanism of lumenogenesis and the function of the proamniotic cavity are still unknown.

Here, we aimed to decipher the mechanism of lumenogenesis and the role of the proamniotic cavity using the 3D ESC model of epiblast development in combination with direct analyses in early mouse embryos. We found that the initiation and expansion of the lumen is driven by the interplay of three processes: vectorial fluid transport, the dynamic exchange of adhesive/antiadhesive factors, and cell division. Furthermore, experimentally blocking lumenogenesis revealed that the proamniotic cavity is an essential structural element that mediates the communication between the embryonic and the extra-embryonic compartments, enabling proper growth and patterning of the early postimplantation embryo.

## RESULTS

### Epiblast morphogenesis and initiation of lumenogenesis

The epiblast lineage originates from the inner (apolar) cells of the E2.5 morula. Thus, in contrast to the outer (TE) cells that have an apical domain defined by the Par complex, the cell membrane of the preimplantation (E4.5) epiblast lacks Par6 expression and shows only basolateral identity (Fig. 1A, left). This naïve pluripotent/apolar state is captured in ESCs grown in 3D culture conditions in the presence of 2i/Lif-supplemented medium (Fig. 1B, left). During the implantation stages, the naïve state is dismantled, and a more developmentally advanced (formative) state of pluripotency is established by E5.5 (6). At the same time, the epiblast undergoes epithelialization, manifested by the de novo formation of a Par6-positive apical domain surrounding the emerging proamniotic cavity (Fig. 1A, right). Similarly, culture of ESCs in medium supplemented with Fgf2/Activin results in the transition into a postimplantation epiblast-like state of pluripotency (7), which, in 3D culture conditions, is associated with the establishment of epithelial polarity and the formation of a

Copyright © 2021  
The Authors, some  
rights reserved;  
exclusive licensee  
American Association  
for the Advancement  
of Science. No claim to  
original U.S. Government  
Works. Distributed  
under a Creative  
Commons Attribution  
NonCommercial  
License 4.0 (CC BY-NC).

<sup>1</sup>Embryonic Self-Organization Research Group, Max Planck Institute for Molecular Biomedicine, Röntgenstraße 20, 48149 Münster, Germany. <sup>2</sup>Transgenic Facility, Max Planck Institute for Molecular Biomedicine, Röntgenstraße 20, 48149 Münster, Germany. <sup>3</sup>Electron Microscopy Facility, Max Planck Institute for Molecular Biomedicine, Röntgenstraße 20, 48149 Münster, Germany. <sup>4</sup>Thermo Fisher Scientific, Achterweg Noord 5, 5651 GG Eindhoven, Netherlands. <sup>5</sup>Flow Cytometry Unit, Max Planck Institute for Molecular Biomedicine, Röntgenstraße 20, 48149 Münster, Germany. \*Corresponding author. Email: ivan.bedzhov@mpi-muenster.mpg.de

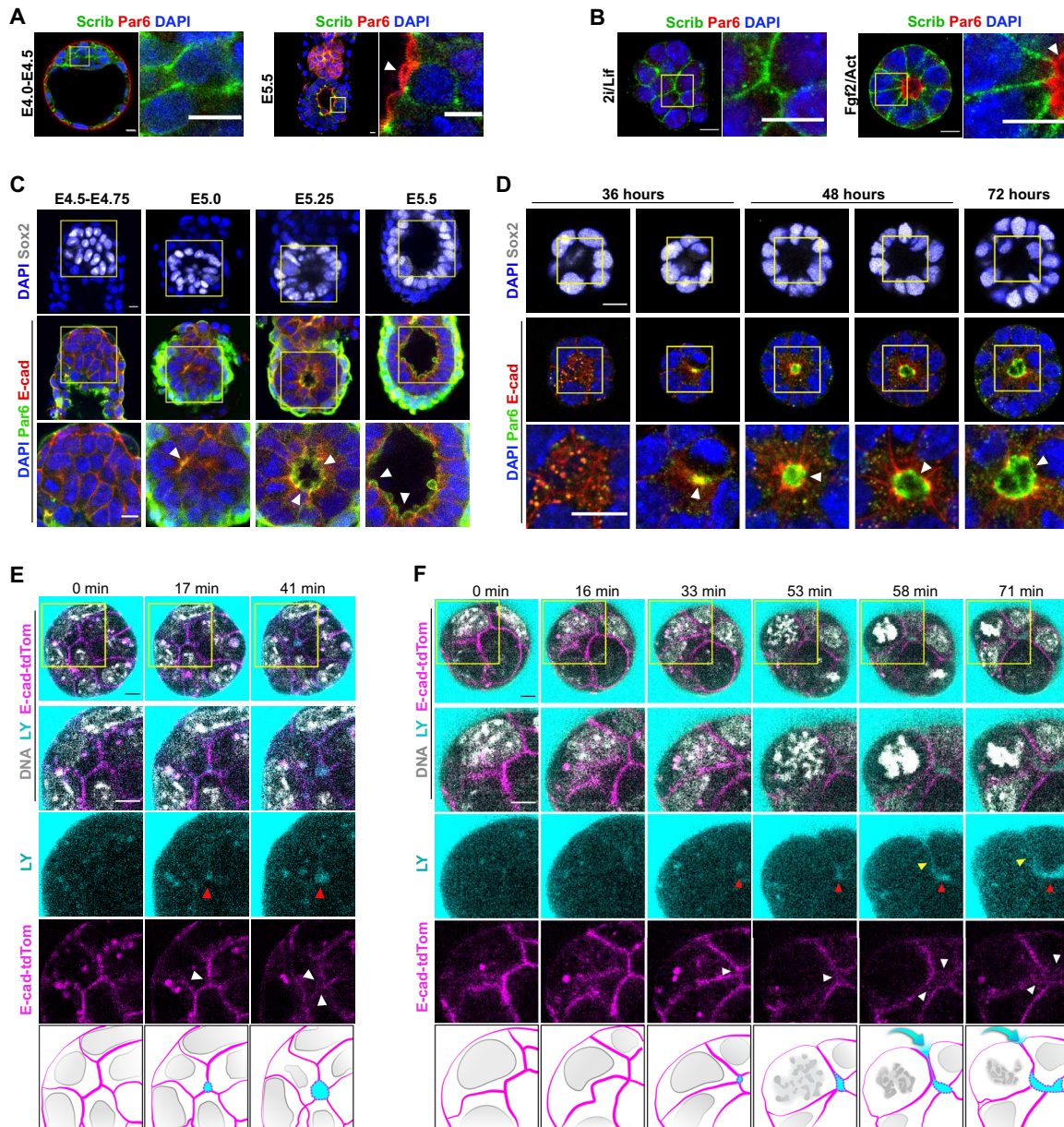


**Fig. 1. Epiblast morphogenesis and initiation of lumenogenesis.** (A) Blastocyst (E4.0-E4.5) and egg cylinder stage (E5.5) embryos stained for the basolateral marker Scrib and the apical marker Par6. Nuclei were counterstained with 4',6-diamidino-2-phenylindole (DAPI). The Par6-positive domain facing the proamniotic cavity in the E5.5 embryo is indicated with a white arrowhead. (B) 3D culture of E14 ESC in N2B27 medium supplemented with 2i/Lif or Fgf2/Activin for 48 hours. The cells were stained for Scrib, Par6, and DAPI. The white arrowhead indicates the Par6-positive apical domain facing the central lumen. (C) E4.5-E5.5 embryos stained for Par6, E-cad, the epiblast marker Sox2, and DAPI. High-magnification images (bottom) show E-cad removal from the apical domain during proamniotic cavity formation (white arrowheads). (D) 3D culture of E14 ESC in N2B27 medium supplemented with Fgf2/Activin for 36, 48, or 72 hours. The cells were stained for Par6, E-cad, Sox2, and DAPI. The E-cad removal from the apical domain is indicated with white arrowheads. (E) Representative images from the time-lapse recording of ESCs expressing E-cad-tdTom grown in 3D culture conditions, in N2B27 medium supplemented with Fgf2/Activin, LY, and DNA live-stain dye Sir-DNA. Lumen initiation is detected by the accumulation of LY (red arrowheads) and decrease of E-cad-tdTom signal (white arrowheads). (F) Representative images from the time-lapse recording of ESCs expressing E-cad-tdTom grown in 3D culture conditions, in N2B27 medium supplemented with Fgf2/Activin, LY, and DNA live-stain dye Sir-DNA. Lumen initiation is detected by the accumulation of LY (red arrowheads) and decrease of E-cad-tdTom signal (white arrowheads). The paracellular fluid transport during mitosis is indicated with yellow arrowheads. Scale bar, 10  $\mu$ m (A to F). Related to fig. S1 and movies S1 and S2.

fluid-filled lumen (Fig. 1B, right). However, how the lumen (proamniotic cavity) is formed in the early postimplantation epiblast is an unsettled fundamental question.

As the formation of the fluid-filled cavity coincides with the establishment of apical-basal polarity, we hypothesized that water

influx splits open the apical membranes in the center of the epiblast to generate the lumen. Therefore, this area should exhibit reduced intercellular adhesion and exhibit reorganization of the cell-cell contacts to facilitate membrane separation. To assess this, we first examined the localization pattern of the major cell adhesion

molecule E-cadherin (E-cad) in relation to the establishment of epithelial polarity in the epiblast. We found that E-cad was uniformly expressed on the cell membrane of the nonpolarized E4.5 epiblast, whereas during the pre- to postimplantation transition, E-cad was absent from the apical membrane and was concentrated on the adherens junctions between neighboring cells (Fig. 1C). This redistribution of E-cad was also faithfully recapitulated *in vitro*, in ESCs grown in 3D culture conditions, between 36 and 72 hours of culture (Fig. 1D and fig. S1A).

To analyze the dynamics of E-cad remodeling during the initiation of lumenogenesis, we generated a reporter ESC line expressing E-cad-tdTomato fusion (E-cad-tdTom). In addition, we supplemented the culture medium with a water-soluble, cell-impermeant tracer [lucifer yellow (LY)] to visualize the emergence of the fluid-filled lumen, and we labeled the nuclei with a live fluorescent dye (SR-DNA) to monitor cell division events. Using live imaging, we found that the E-cad-tdTom signal decreases in the center of the ESC clump, at the site of lumen initiation marked by LY (Fig. 1, E and F; fig. S1, B and C; and movies S1 and S2). The lumen emerged in clumps where, at the time, there were no dividing cells (Fig. 1E and movie S1) and in clumps where some cells were undergoing mitosis (Fig. 1F and movie S2). During cell division, we detected that paracellular fluid contributed to the expansion of the lumen (Fig. 1F, yellow arrowheads). Together, these observations indicate that E-cad removal from the apical membranes defines a site of low intercellular adhesion where water influx opens intermembranous space initiating the formation of the lumen, which expands during cell division. Therefore, we further dissected the interplay between cell adhesion, vectorial fluid transport, and mitosis as the potential underlying processes that drive lumen formation.

### Reorganization of E-cad intercellular adhesion during lumenogenesis

In epithelial cells, E-cad removal from the apical membrane is determined by a highly conserved 21–amino acid sequence in the cytoplasmic portion, recognized by ankyrin-G and clathrin. Mutations in this sequence, abolishing binding of ankyrin-G and engagement of the clathrin endocytosis system, result in E-cad retention on the apical domain (8). To understand whether this mechanism is involved in E-cad removal from the apical domain in the pluripotent lineage, we generated an ESC line that expresses the mutated form of E-cad (8) fused to green fluorescent protein (GFP) (E-cad-LP-GFP; Fig. 2A). In contrast to control cells that expressed wild-type E-cad tagged with GFP (E-cad-WT-GFP), the E-cad-LP-GFP was retained on the apical membrane, colocalizing with the Par6 expression domain (Fig. 2, B and C). The stabilization of E-cad-LP-GFP on the apical interface resulted in delayed lumen opening and an overall decrease in the lumen volume during the 36 to 72 hours period of 3D culture (Fig. 2, C and D).

Next, we analyzed the effects of E-cad retention on the apical membrane in the context of the developing embryo. We used the tetraploid complementation assay, in which ESCs expressing the E-cad-WT-GFP or E-cad-LP-GFP constructs were aggregated with tetraploid morulae to form chimeric embryos. After the chimeric embryos were transferred into recipient mothers, they were later isolated at the early egg cylinder stage (Fig. 2E). The pluripotent lineage in these embryos was established exclusively from the donor cells, thereby enabling epiblast-specific expression of E-cad-WT-GFP or E-cad-LP-GFP. Similar to the expression pattern in the 3D

ESC culture, E-cad-WT-GFP localized on the adherens junctions between neighboring cells (Fig. 2F), whereas E-cad-LP-GFP accumulated apically, resulting in a delay of lumen initiation at E5.25 (Fig. 2, G and H).

Together, these analyses indicate that reorganization of intercellular adhesion, as mediated by E-cad, contributes to the initiation of lumenogenesis. However, even when E-cad was retained, as for the E-cad-LP-GFP-expressing cells both *in vitro* and *in vivo*, the lumen did form (albeit with a delay), suggesting that antiadhesive factors are at play during the process of apical membrane separation.

### The exchange of apical E-cad expression with apical expression of CD34 family antiadhesins facilitates membrane separation

In cysts of Madin-Darby canine kidney cells, as well as in the developing mouse aorta and kidney glomerular cells, the antiadhesive molecule podocalyxin (Podxl) mediates membrane hollowing through charge repulsion via its highly negatively charged glycosylated and sialylated extracellular domain (9–11). Such role of Podxl was previously suggested in the pluripotent lineage but not approached genetically (2, 12). To understand whether Podxl function is required for the formation of the proamniotic cavity, first, we analyzed Podxl expression in relation to E-cad distribution during the blastocyst-to-egg cylinder transition. At the blastocyst stage, the epiblast was negative for Podxl and exhibited uniform E-cad expression on the cell membrane. Between E5.0 and E5.5, Podxl and E-cad displayed a mutually exclusive pattern: E-cad was expressed on the lateral cell-cell contacts, whereas Podxl localized on the apical domain (Fig. 3A). This exchange of adhesive (E-cad) for antiadhesive (Podxl) factors on the lumen-enclosing membrane was also faithfully recapitulated *in vitro*, in the 3D ESC culture (Fig. 3B).

Podxl belongs to the CD34 family of transmembrane antiadhesins that consists of three members: CD34, Podxl, and endoglycan (Podxl2). We found that all members of the CD34 family are transcriptionally up-regulated during the transition from a nonpolarized to a polarized state in 3D culture conditions (Fig. 3C). As the charge repulsion force governed by the extracellular domain of these proteins has a short distance effect, we hypothesized that the CD34 antiadhesins may play a role in the lumen initiation phase. However, none of the reported single knockouts of the CD34 family members exhibit embryonic defects (13–15), which suggests functional redundancy. Therefore, we generated a CD34, Podxl, and endoglycan triple-knockout ESC line using the CRISPR-Cas9 genome editing approach (Fig. 3D and fig. S2A) and analyzed the lumen formation in two individual clones. In comparison to WT (control) cells, in the two triple-knockout clones, we found a delay in apical membrane hollowing between 36 and 48 hours of culture and a consistent decrease of the lumen volume at 48 to 72 hours (Fig. 3, E and F). This shows that the CD34 family of antiadhesins facilitates apical membrane separation during the onset of lumenogenesis, but their function is not critical for lumen formation *per se*. Accordingly, we found that the proamniotic cavity is also formed *in vivo*, using the tetraploid complementation assay, where the triple-knockout ESCs were used to generate epiblast-specific depletion of the CD34 family (Fig. 3, G and H, and fig. S2B).

To understand the extent to which the exchange of apically localized E-cad with the antiadhesins affects lumenogenesis, we expressed E-cad-LP-GFP in control (WT) or CD34 triple-knockout cells. As expected, when combining the CD34 family depletion with

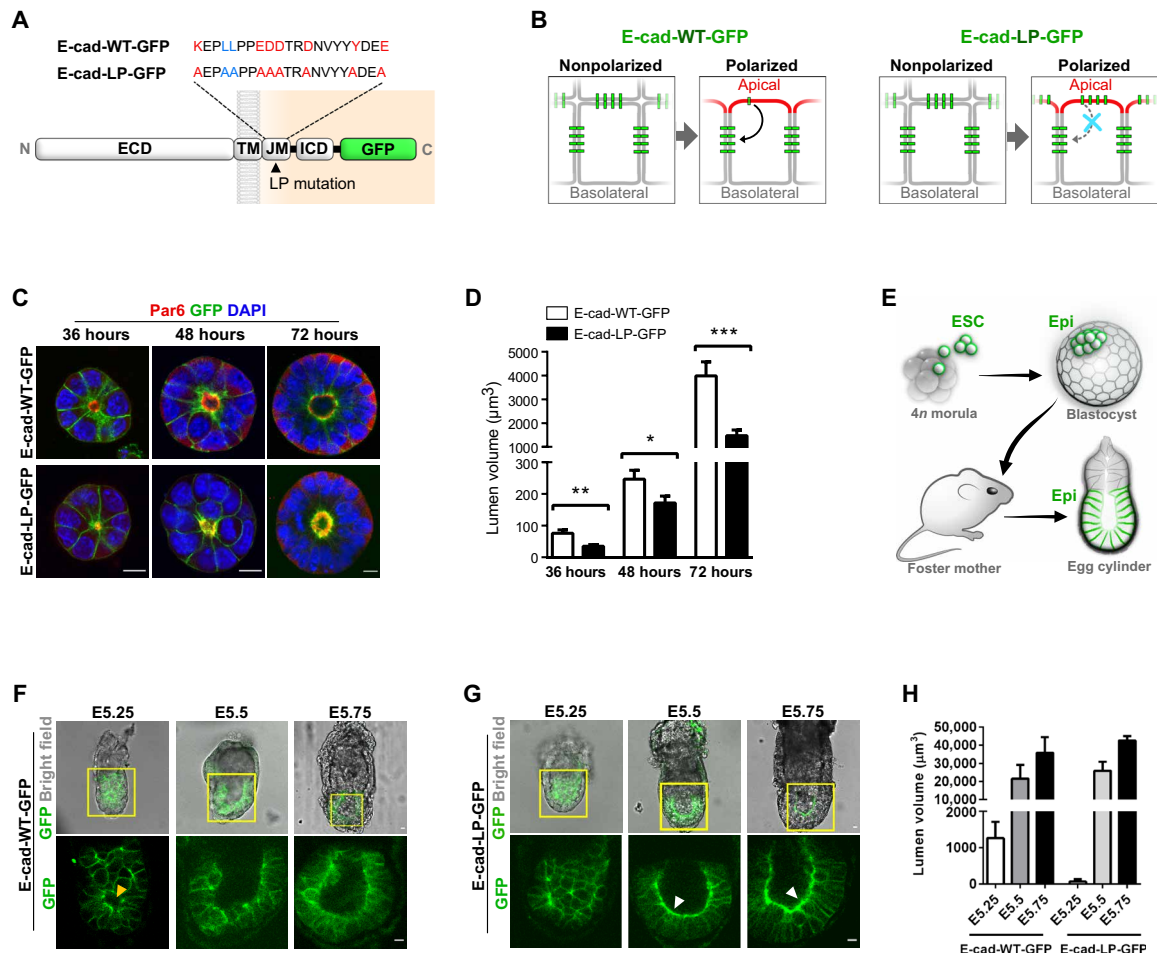


**Fig. 2. Reorganization of E-cad intercellular adhesion during lumenogenesis.** (A) Schematic representation of the E-cad-WT-GFP and E-cad-LP-GFP constructs. Amino acid mutations in the juxtamembrane domain (JM) of E-cad-LP-GFP are shown. Amino acid sequences in red are required for ankyrin-G binding, and amino acid sequences in blue are required for clathrin-dependent endocytosis. ECD, ectodomain; TM, transmembrane domain; ICD, intracellular domain. (B) Schematic representation of trafficking of WT E-cad-WT-GFP (left) and the endocytosis-deficient mutant E-cad-LP-GFP (right). (C) ESCs expressing E-cad-WT-GFP or E-cad-LP-GFP cultured in N2B27 medium supplemented with Fgf2/Activin for 36, 48, or 72 hours. The cells were stained for GFP and Par6. Nuclei were counterstained with DAPI. (D) Quantification of the lumen volume from (C) based on Par6 staining, at least three independent experiments for each time point (36 hours,  $n > 25$ ; 48 hours,  $n > 39$ ; 72 hours,  $n > 72$ ). Error bars represent SEM.  $P$  value was calculated using unpaired Student's  $t$  test. \* $P < 0.05$ ; \*\* $P < 0.01$ ; \*\*\* $P < 0.001$ . (E) Schematic representation of the tetraploid complementation assay. (F) Live-microscopy images of egg cylinder stage embryos ( $n = 21$ ) generated following tetraploid complementation using E-cad-WT-GFP-expressing ESCs. The emerging proamniotic cavity is marked with yellow arrowhead. (G) Live-microscopy images of egg cylinder stage embryos ( $n = 12$ ) generated following tetraploid complementation using E-cad-LP-GFP-expressing ESCs. The apical localization of E-cad-LP-GFP is marked with white arrowheads. (H) Quantification of the lumen volume from (F) and (G) (E-cad-WT-GFP-E5.25,  $n = 15$ ; E5.5,  $n = 4$ ; E5.75,  $n = 2$ ; E-cad-LP-GFP-E5.25,  $n = 5$ ; E5.5,  $n = 5$ ; E5.75,  $n = 2$ ). Error bars represent SEM. Scale bar, 10  $\mu\text{m}$  (C, F, and G).

the E-cad retention in E-cad-LP-GFP-expressing cells, we observed a further reduction in the lumen volume (fig. S2, C and D). Nevertheless, lumen formation was not abolished. This indicates that the influx of water observed in the live imaging experiments (Fig. 1, E and F) is sufficient to overcome the adhesive force of E-cad and hollow the apical membranes, even in the absence of the antiadhesive factors.

### Water influx via osmotic gradients generated by combined activity of $\text{Na}^+/\text{K}^+$ and $\text{Cl}^-$ pumps initiates lumen formation

The initial live imaging analyses indicated that the lumen can emerge when cells are not undergoing mitosis as well as during cell division (Fig. 1, E and F). As cell division is coupled with paracellular fluid transport that contributes to the lumen volume, this suggests that water influx can occur via two ways: one that is mediated by cell division, where water can flow between neighboring cells during

proliferation, and one that is not necessarily associated with cell division, potentially driven via the establishment of osmotic gradients.

To examine the potential role of osmotic gradients, we characterized the expression pattern of  $\text{Na}^+/\text{K}^+$  [ $\text{Na}^+$ - and  $\text{K}^+$ -dependent adenosine triphosphatase ( $\text{Na}^+/\text{K}^+$ -ATPase)] and  $\text{Cl}^-$  [cystic fibrosis transmembrane conductance regulator (CFTR)] pumps, as they were previously shown to be involved in the formation of the blastocyst cavity during the preimplantation stages (16, 17). We found that both ion pumps, including aquaporin channels such as aquaporin 4 (Aqp4), were expressed in the early postimplantation epiblast, as well as in vitro in the 3D ESC culture (Fig. 4A and fig. S3A). Treatment with Aqp inhibitors resulted in a moderate decrease of the lumen volume at 72 hours of 3D culture (figs. S3, B to E). Separate treatment with pharmacological inhibitors of  $\text{Na}^+/\text{K}^+$ -ATPase or CFTR decreased the lumen volume, whereas combined inhibition almost diminished lumen

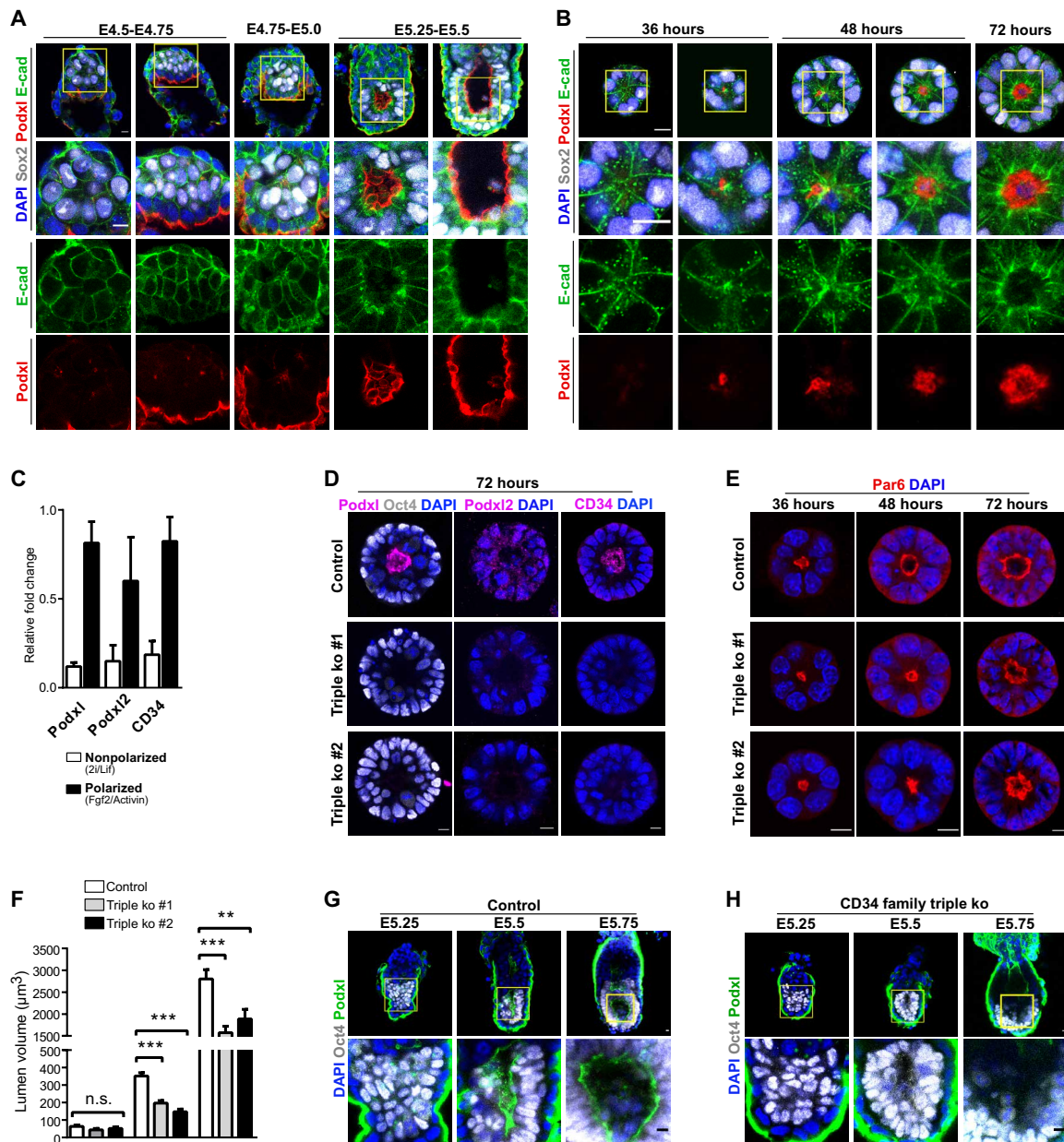


**Fig. 3. The CD34 family antiadhesins facilitates membrane separation.** (A) E4.5-E5.5 embryos stained for E-cad, Podxl, and epiblast lineage marker Sox2. Nuclei were counterstained with DAPI. (B) 3D culture of E14 ESC in N2B27 medium supplemented with Fgf2/Activin for 36, 48, or 72 hours and stained for E-cad, Podxl, Sox2 and DAPI. (C) Reverse transcription polymerase chain reaction analysis of Podxl, Podxl2, and CD34 expression of E14 ESCs 3D cultured for 48 hours in N2B27 medium supplemented with 2i/Lif or Fgf2/Activin. (D) 3D culture of E14 ESC (control) and CD34 family triple-knockout ESC in N2B27 medium supplemented with Fgf2/Activin for 72 hours. The cells were stained for Podxl, Podxl2, and CD34, and Oct4 and DAPI. (E) 3D culture of E14 ESC (control) and CD34 family triple-knockout ESC in N2B27 medium supplemented with Fgf2/Activin. The cells were stained for Par6 and DAPI and 36, 48, or 72 hours of culture. (F) Quantification of lumen volume from (E) based on Par6 staining; at least three independent experiments (36 hours,  $n > 14$ ; 48 hours,  $n > 73$ ; 72 hours,  $n > 115$ ). Error bars represent SEM.  $P$  value was calculated using one-way analysis of variance (ANOVA) with a Tukey's post hoc test.  $^{***}P < 0.01$ ;  $^{****}P < 0.001$ . n.s., not significant. (G) Egg cylinder stage embryos ( $n = 10$ ) generated following tetraploid complementation using control E14 ESC and stained for Podxl, Sox2, and DAPI. (H) Egg cylinder stage embryos ( $n = 15$ ) generated following tetraploid complementation using CD34 family triple-knockout ESC and stained for Podxl, Sox2, and DAPI. Note that Podxl is expressed only in the extraembryonic lineages, the extraembryonic ectoderm and visceral endoderm, but not in the epiblast. Scale bar, 10  $\mu\text{m}$  (A, B, D, E, G, and H). Related to fig. S2.

formation at 36 to 48 hours and drastically reduced the lumen volume at 72 hours of 3D culture (Fig. 4, B and C).

Next, we treated the CD34 family triple-knockout cells expressing E-cad-LP-GFP with a combination of  $\text{Na}^+/\text{K}^+$ -ATPase and CFTR inhibitors, which suppressed lumen formation at 36 to 48 hours of

culture (Fig. 4, D and E). Live imaging of control (untreated) E-cad-LP-GFP<sup>+</sup>/CD34 family knockout cells revealed that the water influx is sufficient to overcome the adhesive strength of E-cad and initiate lumenogenesis (Fig. 4F and movie S3). In contrast, inhibiting  $\text{Na}^+/\text{K}^+$ -ATPase and CFTR halted membrane separation and lumen

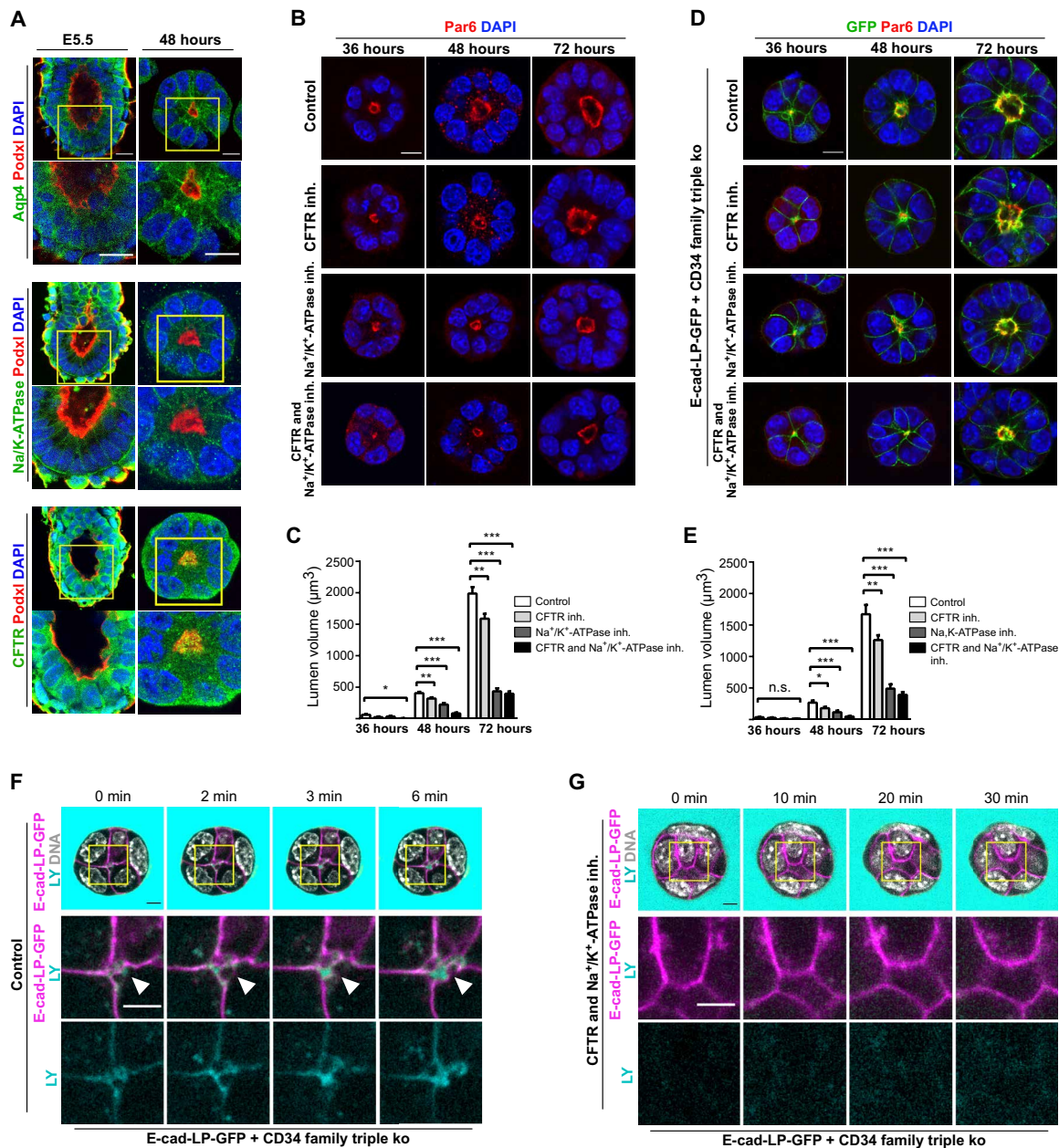


**Fig. 4. Fluid influx via osmotic gradients initiates lumen formation.** (A) E5.5 embryos (left) and 3D cultured ESCs stained for Podxl and  $\text{Na}^+/\text{K}^+$ -ATPase, CFTR, or Aqp4. (B) 3D culture of E14 ESCs in N2B27 supplemented with Fgf2/Activin. The CFTR inhibitor CFTR(inh)-172 (10 nM) and/or  $\text{Na}^+/\text{K}^+$ -ATPase inhibitor ouabain (100  $\mu\text{M}$ ), were added from 24 hours of culture. (C) Quantification of lumen volume from (B) based on Par6 staining; at least three independent experiments (36 hours,  $n > 6$ ; 48 hours,  $n > 49$ ; 72 hours,  $n > 48$ ). Error bars represent SEM.  $P$  value was calculated using one-way ANOVA with a Tukey's post hoc test.  $*P < 0.05$ ;  $**P < 0.01$ ;  $***P < 0.001$ . (D) 3D culture of CD34 family triple-knockout ESCs expressing E-cad-LP-GFP in the presence of CFTR inhibitor and/or  $\text{Na}^+/\text{K}^+$ -ATPase inhibitor. (E) Quantification of lumen volume from (D) based on Par6 staining; at least three independent experiments (36 hours,  $n > 11$ ; 48 hours,  $n > 22$ ; 72 hours,  $n > 54$ ). Error bars represent SEM.  $P$  value was calculated using one-way ANOVA with a Tukey's post hoc test.  $*P < 0.05$ ;  $**P < 0.01$ ;  $***P < 0.001$ . (F) Still images of the time-lapse microscopy of CD34 family triple-knockout cells expressing E-cad-LP-GFP. The site of lumen formation is indicated with a white arrowhead. (G) Still images of the time-lapse microscopy of CD34 family triple-knockout cells expressing E-cad-LP-GFP in the presence of the CFTR inhibitor and  $\text{Na}^+/\text{K}^+$ -ATPase inhibitor. Scale bar, 20  $\mu\text{m}$  [A (embryo)] and 10  $\mu\text{m}$  [A (ESCs), B, D, F, and G]. Related to fig. S3 and movies S3 to S5.

enlargement within the 36- to 48-hour time frame (Fig. 4, D and G, and movie S4). Between 48 and 72 hours, as the cells kept on multiplying, a small lumen expanded even the presence of  $\text{Na}^+/\text{K}^+$ -ATPase and CFTR inhibitors (Fig. 4, D and E). Live imaging of CD34 family triple-knockout cells expressing E-cad-LP-GFP in the presence of  $\text{Na}^+/\text{K}^+$ -ATPase and CFTR inhibitors at 72 hours of culture revealed paracellular water influx during cell division, indicating that cell

proliferation and lumenogenesis are interconnected (fig. S3F and movie S5).

### Paracellular fluid transport during cell division mediates lumen expansion

To analyze the dynamics of fluid transport during cell division, we live-imaged ESCs expressing nuclear (Histone H2B-tdTomato) and

membrane (E-cad-WT-tdTomato) markers in the presence of a fluid tracer (LY). We determined that the 3D ESC model, similar to the postimplantation epiblast, is a pseudostratified epithelium that, in the process of cell division, exhibits interkinetic nuclear migration. The time-lapse imaging revealed that cells initiating mitosis round up and move apically. During metaphase and anaphase, water enters between the mitotic cell and its neighbors and contributes to the expanding cavity. Subsequently, during telophase, paracellular pockets of water follow the cleavage furrow and merge with the central lumen (Fig. 5A and movie S6). Thereby, the mitosis-associated paracellular flow results in an increase in the lumen volume (fig. S4A). Similarly, imaging E5.5 embryos expressing membrane tdTomato confirmed that paracellular water influx during cell division contributes to the proamniotic cavity in vivo (Fig. 5B and movie S7).

Next, in search of intermembranous spaces indicative of paracellular fluid transport, we examined the ultrastructure of the pluripotent lineage using transmission electron microscopy. We found that the cells of the E4.5 epiblast were tightly packed, including the cells undergoing mitosis (Fig. 5C, left). In contrast, at the egg cylinder stage, multiple microlumens were visible between the cells in addition to the larger proamniotic cavity in the center of the epiblast (Fig. 5C, middle). Similarly, we detected intercellular spaces in the ESC clumps grown in 3D culture conditions (Fig. 5C, right).

As conventional transmission electron microscopy provides limited 2D information, we used 3D electron microscopy to analyze the structure of the lumen and the intermembranous spaces in the nearby vicinity. We observed an intermembranous network connected to the central cavity as well as multiple small pockets between the cells (Fig. 5D and movie S8). Moreover, in accord with the live imaging experiments, we found intermembranous pockets at the cleavage furrow in cells at telophase (Fig. 5E).

To analyze the contribution of fluid flow during mitosis, we treated cells with a low concentration of nocodazole to arrest the cell cycle at metaphase. We performed electron microscopy of these cells and found multiple intermembranous spaces between cells in metaphase and their neighbors (fig. S4B). Live imaging of control (untreated) cells and cells cultured in the presence of nocodazole confirmed that the cells in metaphase exhibit paracellular water flow (fig. S4, C and D). Accordingly, the lumen volume in nocodazole-treated samples was larger than that of the control (untreated) ESC clumps, whereas treatment with myc inhibitor, which enriches ESCs at G1 phase (18), resulted in a smaller lumen volume (fig. S4, E to G). Together, this shows that the paracellular water influx during cell division contributes to the expansion of the lumen. This type of fluid transport, to our best knowledge, has not been described so far in other model systems.

### Water influx from the blastocoel fills up the proamniotic cavity

Next, we sought to identify the source of fluid that fills up the proamniotic cavity. To this end, we examined the structure of intact E4.75 and E5.5 embryos within the surrounding maternal tissues. Whole-mount deciduae containing the sequential stages of peri-implantation embryos were subjected to a tissue clearing procedure, rendering the material completely transparent. The samples were stained for laminin and Podxl to delineate the blastocoel (blastocyst cavity) and the proamniotic cavity. Laminin expression was predominant on the mural TE/Reichert's membrane, as well as in the PE/visceral endoderm (E4.75/E5.5), thereby outlining the

blastocoel, whereas Podxl was expressed on the cell membrane surrounding the proamniotic cavity in the center of the epiblast. In addition, Podxl was also localized on the apical domain of the PE (E4.75) and visceral endoderm (E5.5), delineating the overall shape of the inner cell mass (ICM) and the egg cylinder, respectively (Fig. 6A).

The in situ analysis of the E4.75 and E5.5 embryos showed that the nascent egg cylinder proliferates into the blastocyst cavity during the peri-implantation stages (Fig. 6, A and B). As the egg cylinder grows into the blastocoel fluid, we hypothesized that the blastocoel is the nearest source of water that could fill up the emerging proamniotic cavity (Fig. 6B). To test this hypothesis, we injected the LY tracer to mark the blastocoel fluid in E4.5 blastocysts as well as in E5.0 and E5.5 egg cylinders with intact Reichert's membranes (Fig. 6C). As expected, the LY injection in the E4.5 embryos marked the blastocyst cavity, and there was no detectable signal in the ICM (Fig. 6C, left). However, marking the blastocoel fluid in E5.0 and E5.5 embryos resulted in a subsequent detection of labeled fluid in the proamniotic cavity (Fig. 6C, yellow arrowheads). Therefore, this indicates that during the peri-implantation stages, the blastocoel supplies fluid that fills up the proamniotic cavity of the emerging egg cylinder.

### The proamniotic cavity acts as a hub mediating embryonic/extraembryonic lineage communication and patterning

So far, our analysis has shown that the water influx can overcome the intercellular adhesion to initiate and expand the proamniotic cavity. Therefore, we hypothesized that strengthening the adhesive properties of E-cad should oppose membrane separation and prohibit lumen formation. To reinforce E-cad binding, we used the streptavidin-biotin interaction approach in the context of the endocytosis-deficient form of E-cad. We generated two E-cad constructs, one containing streptavidin conjugated to the E-cad ectodomain and C-terminal GFP tag (E-cad-strep-LP-GFP) and another containing the biotinylation sequence in the ectodomain and tdTomato at the C terminus (E-cad-bio-LP-tdTom). We generated a stable ESC line coexpressing both variants of E-cad, together with a construct encoding Cerulean-tagged biotin ligase (BirA-Cerulean). Thus, in the presence of biotin, BirA biotinylates the tdTomato-tagged E-cad, enabling a strong interaction between it and the GFP-tagged streptavidin-conjugated E-cad (Fig. 7, A and B).

Next, we analyzed lumen formation in 3D culture, comparing cells grown in medium supplemented with biotin to control (untreated) ESCs and found that lumenogenesis was completely suppressed in the biotin-treated samples (Fig. 7, C and D). Although the cavity was not formed, the general epithelial organization in these cells was properly established: The nucleus was positioned basally, whereas Golgi and filamentous actin were concentrated apically (Fig. 7C). Moreover, both the biotin-treated and untreated cells maintained Oct4 expression and down-regulated Nanog within 48 hours of culture, indicating proper exit of naive pluripotency (Fig. 7C). In addition, we examined the ultrastructure of these cells using electron microscopy and confirmed that the enforcement of E-cad contacts abolished lumen formation and prevented the establishment of intermembranous spaces between cells, including the ones undergoing mitosis (Fig. 7E).

Last, we used this system to block the formation of the proamniotic cavity in the context of the embryo and analyze the potential effects on early postimplantation embryogenesis. First, we checked whether

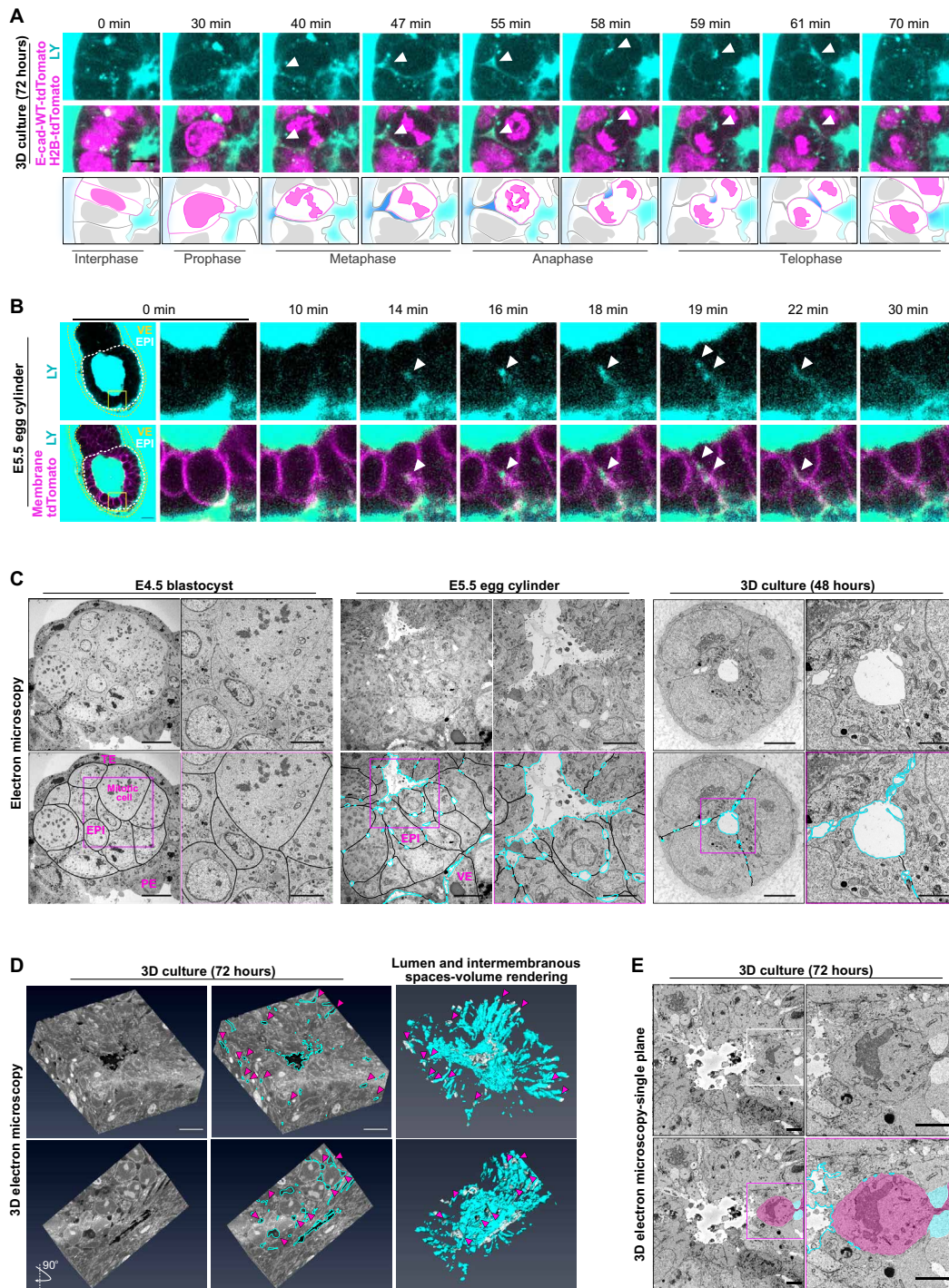


**Fig. 5. Paracellular fluid transport mediates lumen expansion during mitosis.** (A) Representative images from time-lapse microscopy of ESCs expressing membrane (E-cad-WT-tdTom) and nuclear (Histone H2B-tdTom) markers. The cells were grown in 3D culture for 72 hours in N2B27 medium supplemented with Fgf2/Activin in the presence of LY. The paracellular fluid flow during the subsequent stages of cell division is indicated with white arrowheads; a schematic of the process is represented on the lower panel. (B) Representative images from the time-lapse microscopy of egg cylinder stage embryos (E5.5) expressing membrane tdTomato. The paracellular transport of LY-marked fluid (cyan) to the proamniotic cavity is visible during cell division (white arrowheads). (C) Transmission electron microscopy images of the epiblast in E4.5 blastocyst, E5.5 egg cylinder, and 3D cultured ESCs for 48 hours. The paracellular spaces and the central cavity are marked with cyan (bottom); EPI, epiblast; VE, visceral endoderm. (D) Serial block-face scanning electron microscopy images of E14 ESCs grown in 3D culture conditions for 72 hours in N2B27 medium supplemented with Fgf2/Activin. Multiple intermembranous spaces (outline in cyan; magenta arrowheads) are visible around the central lumen. 3D volume rendering of the lumen and intermembranous spaces (outer surface, cyan; inner surface, gray). (E) Single plane of serial block-face scanning electron microscopy showing cells in telophase (magenta) and intermembranous pockets at the cleavage furrow (cyan). Scale bar, 10  $\mu$ m (A and D); 20  $\mu$ m (B); 10 and 5  $\mu$ m [C (left and middle)] and 5 and 2  $\mu$ m [C (right)]; and 5  $\mu$ m (E). Related to fig. S4 and movies S6 to S8.

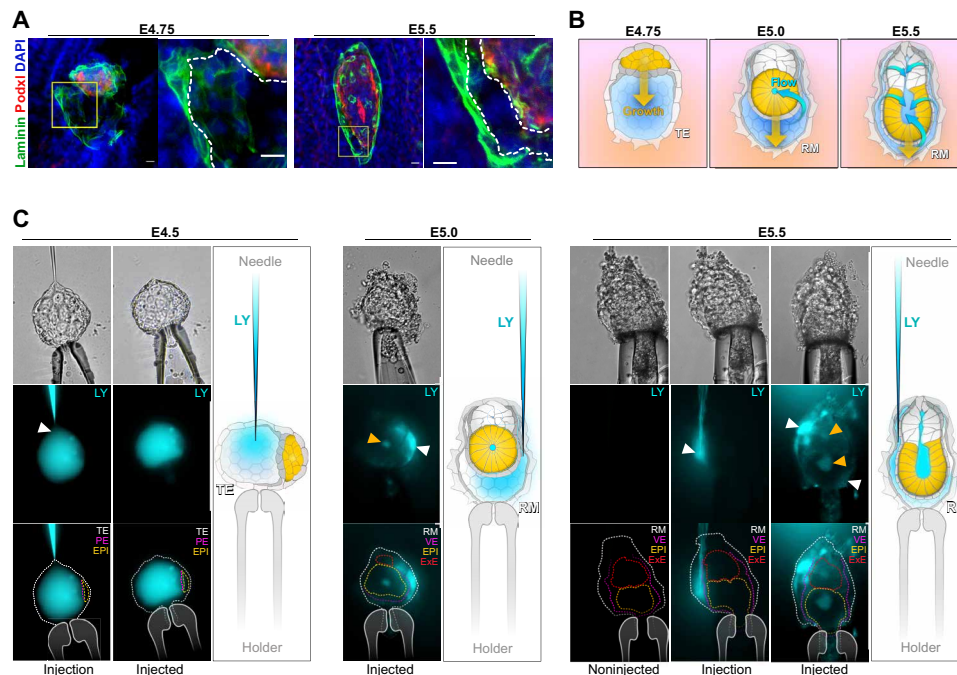


**Fig. 6. The proamniotic cavity fluid is supplied by the blastocoel.** (A) Whole-mount deciduae containing E4.75 and E5.5 embryos subjected to tissue-clearing procedure and stained for laminin and Podxl. Nuclei were counterstained with DAPI; the blastocoel is marked with a white line. The images are composed of several combined (projected) optical sections. The scattered laminin-positive cells at E5.5 are parietal endoderm cells of the enveloping Reichert's membrane. (B) Schematic representation of blastocyst to egg cylinder growth and morphogenesis with blue arrows indicating the flow of blastocoel fluid into the emerging proamniotic cavity. The epiblast is marked with yellow, the extraembryonic ectoderm with white, and the primitive/visceral endoderm with gray; RM, Reichert's membrane. (C) Still images of LY microinjection marking the blastocoel fluid in E4.5, E5.0, and E5.5 embryos. TE (white); RM (white), Reichert's membrane; EPI (yellow), epiblast; PE (magenta), visceral endoderm; ExE (red), extraembryonic ectoderm. A white arrowhead refers to the site of microinjection, and a yellow arrowhead refers to the proamniotic cavity. Scale bar, 10  $\mu$ m (A).

biotin treatment per se has an effect on embryonic development. We treated mice with biotin and isolated WT embryos at E5.5. The embryos exposed to biotin were indistinguishable from the nontreated control embryos (fig. S5A). Next, we used the tetraploid complementation assay to incorporate the ESCs, and after transferring the chimeric embryos into control (untreated) or biotin-treated recipient mothers, the embryos were isolated at the early egg cylinder stage. As the epiblast in these embryos was established exclusively from the donor cells, the strengthening of E-cad adhesion was limited only to the embryonic lineage. Accordingly, the E5.5 embryos showed expression of the GFP- and tdTomato-tagged E-cad variants in an epiblast-specific manner, resulting in the absence of proamniotic cavity formation in embryos exposed to biotin (Fig. 7F). In both groups, the epiblast was positive for the pluripotency marker Oct4 (fig. S5, B and C), but the embryos lacking a proamniotic cavity had an overall smaller in size. These embryos showed reduced proliferation based on phospho-histone H3 staining, which was not associated with an increase in apoptosis (fig. S5, D to G). This phenotype was reminiscent of the reduced growth previously reported in Nodal signaling mutants (19–23).

Nodal activity in the early postimplantation embryo orchestrates the processes of axis formation and loss of Nodal results in a developmental arrest before gastrulation (19, 24). At E5.5, Nodal is required for the induction of the distal visceral endoderm (DVE), which, in turn, expresses Nodal antagonists such as Cerberus1 (Cer1), thereby establishing a proximal-distal gradient of Nodal activity. Subsequently, the DVE migrates to one side of the egg cylinder forming the anterior visceral endoderm (AVE), which defines the anterior region of the underlying epiblast, whereas Nodal activity on the opposite, posterior

region is required for formation of the primitive streak. Thus, in addition to their reduced size, Nodal-deficient embryos exhibit loss of DVE/AVE and posterior epiblast markers (19, 24).

To understand whether embryos without a proamniotic cavity display features of impeded Nodal signaling, we analyzed the expression pattern of the DVE/AVE marker Cer1 and the primitive streak marker T-brachyury (T-bry). We found that in E5.5 control embryos, Cer1 was expressed in the visceral endoderm, at the distal tip of the egg cylinder, whereas T-bry was detectable in the posterior epiblast at E6.5 (Fig. 7, G and H). In contrast, embryos lacking a proamniotic cavity showed no expression of DVE and primitive streak markers (Fig. 7, G and H), indicating that the proximal-distal and, consequently, the anterior-posterior axes were not properly specified.

Nodal is produced in the epiblast and is secreted as a precursor protein that is processed by Furin and PACE4 (subtilisin-like pro-protein convertase 4) endoproteases, which are expressed in the extraembryonic ectoderm (ExE). It has been reported that Furin and PACE4 are released by the ExE to exert their activity on Nodal in the epiblast, and moreover, a Furin-GFP fusion protein was found to accumulate in the proamniotic cavity (21, 25). To test whether Nodal is also released in the cavity, we generated ESCs expressing full-length Nodal protein tagged with GFP (GFP-Nodal) and marked the cell membrane with E-cad-WT-tdTomato. We incorporated these cells into preimplantation embryos via morula aggregation, and later, at the egg cylinder stage, we detected a GFP-Nodal signal in the proamniotic cavity (Fig. 7I). This finding indicates that the cavity is a microenvironment where Nodal and the protease required to process the Nodal proprotein into an active form are pooled together into the luminal

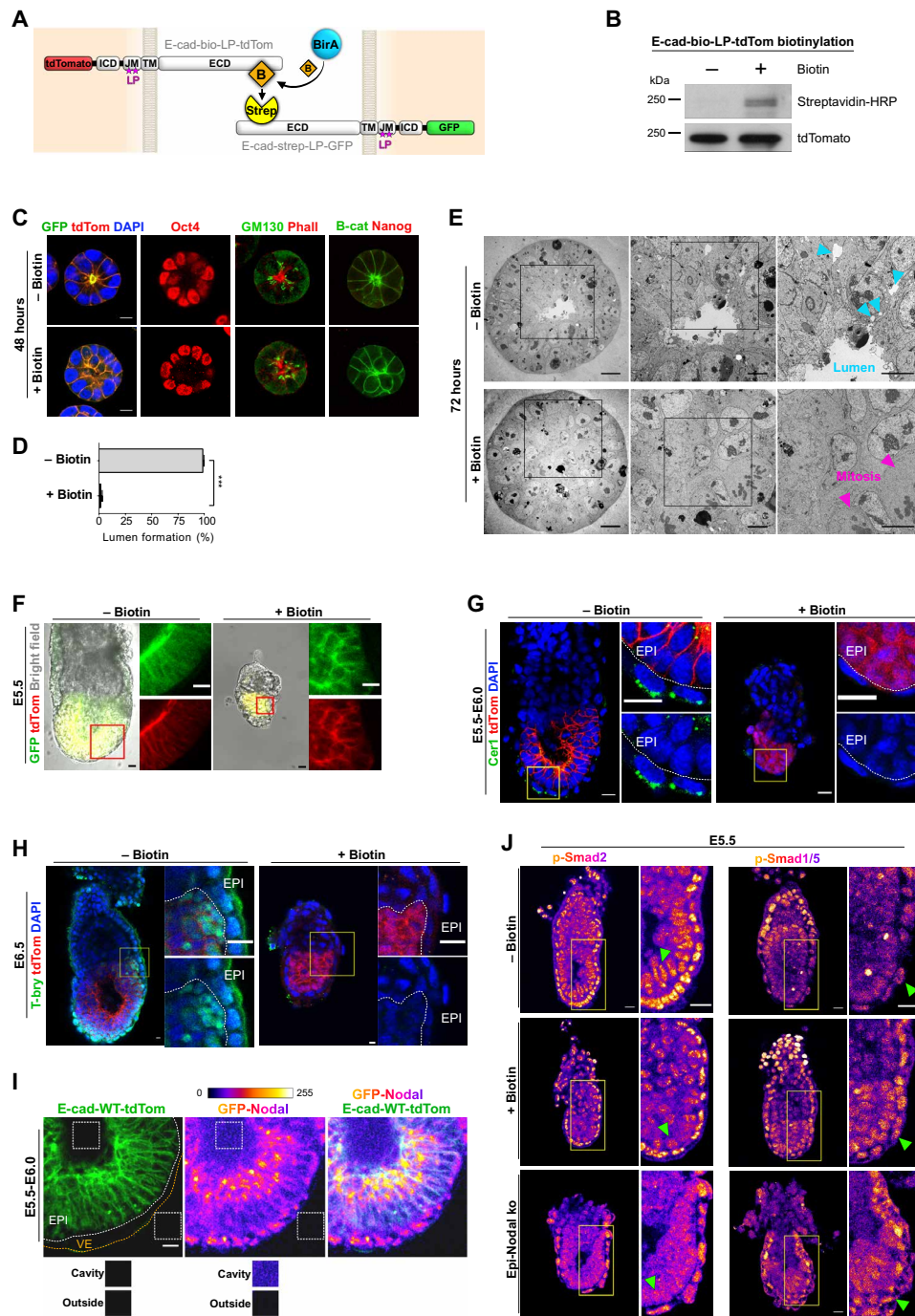


**Fig. 7. The proamniotic cavity is required for lineage communication and patterning of the early postimplantation embryo.** (A) Schematic representation of the biotin-streptavidin interaction used to strengthen E-cad-mediated intercellular adhesion. (B) Western blot analysis of E-cad-bio-LP-tdTom biotinylation using streptavidin-HRP (horseradish peroxidase) antibody; the tdTomato tag was detected using anti-RFP antibody and used as a loading control. (C) 3D culture of ESCs expressing the E-cad biotin-streptavidin adhesion system. (D) Quantification of the lumen formation in (C) based on Par6 staining; at least three independent experiments ( $n > 132$ ). Error bars represent SEM;  $P$  value was calculated using unpaired Student's  $t$  test.  $***P < 0.001$ . (E) Transmission electron microscopy of ESCs expressing the E-cad biotin-streptavidin adhesion system. (F) Embryos generated following tetraploid complementation using ESCs expressing the biotin-streptavidin adhesion system. Control embryos ( $n = 27$ ) and embryos derived from foster mothers exposed to biotin ( $n = 12$ ). (G) E5.5 control embryos ( $n = 15$ ) and embryos derived from foster mothers exposed to biotin ( $n = 12$ ) stained for Cer1, tdTomato, and DAPI. (H) E6.5 control embryos ( $n = 16$ ) and embryos derived from foster mothers exposed to biotin ( $n = 13$ ) stained for T-bry, tdTomato, and DAPI. (I) Live-microscopy images of egg cylinder stage embryo (E5.5-E6.0) generated following morula aggregation with ESCs expressing E-cad-WT-tdTom and GFP-Nodal and cultured in vitro to egg cylinder stage ( $n = 9$ ). (J) Control embryos (p-Smad2 stained,  $n = 9$ ; p-Smad1/5 stained,  $n = 7$ ), embryos derived from biotin-treated foster mothers (p-Smad2 stained,  $n = 8$ ; p-Smad1/5 stained,  $n = 11$ ), and Epi-Nodal ko embryos (p-Smad2 stained,  $n = 11$ ; p-Smad1/5 stained,  $n = 10$ ). Scale bar, 10  $\mu\text{m}$  [C, E (left), F, H, and I]; 5  $\mu\text{m}$  [E (middle and right)]; and 20  $\mu\text{m}$  (G and J). Related to fig. S5.

fluid. Thus, failure to form the proamniotic cavity can impede Nodal signaling, resulting in growth retardation and failure to properly establish the early body axes.

Nodal binds to type I and II receptors, which activate Smad2 and Smad3 of the Tgf $\beta$  pathway and loss of Nodal is associated with decreased Smad2 phosphorylation in the epiblast at E5.5 (21, 26). pSmad2 is still present in the visceral endoderm of Nodal KO embryos, as Activin and potentially Gdf1 and Gdf3 were suggested induce Smad2 phosphorylation in this compartment in the absence of Nodal (26–29). We stained for pSmad2 control embryos (–biotin) and embryos without proamniotic cavity (+biotin) and found reduced pSmad2 signal in the epiblast of embryos exposed to biotin. In accord with the Nodal ko phenotype, pSmad2 was still present in the visceral endoderm of embryos lacking proamniotic cavity (Fig. 7J, left). Alongside, we generated epiblast-specific Nodal loss of function (Epi-Nodal ko) by aggregating tetraploid morulae with Nodal ko ESCs [Nodal<sup>lacZ/lacZ</sup> (30)]. At E5.5, the Epi-Nodal ko embryos were smaller and also exhibited reduced Smad2 phosphorylation in the epiblast compared to the control embryos (Fig. 7J, left).

Proper DVE specification requires limiting the antagonistic activity of the Bmp/pSmad1,5,9 pathway in the embryonic portion of the visceral endoderm (26). In Nodal ko, as well as in Smad2/3 ko embryos, pSmad1,5,9 levels are aberrantly elevated in the visceral endoderm, which, in turn, inhibits DVE specification (26, 31, 32). Similarly, we found elevated pSmad1,5 signal in the visceral endoderm and epiblast of Epi-Nodal ko mutants and embryos lacking proamniotic cavity (+biotin), in comparison to control embryos (Fig. 7J, right). Together, this shows that the proamniotic cavity is required for the adequate function of signaling gradients, establishment of signaling centers and proper patterning of the postimplantation embryo.

## DISCUSSION

The mammalian development at the time of implantation is largely unexplored and is probably the most enigmatic period of early

embryogenesis. During the peri-implantation stages, the mouse embryo radically changes its appearance, transforming from a hollow-shaped blastocyst to a tube-like conceptus (egg cylinder). The core of the egg cylinder is composed of a fluid-filled cavity, whose function and mechanism of formation have been elusive so far. Here, we dissected the processes that drives lumenogenesis and established a model to describe the generation and function of the proamniotic cavity (Fig. 8).

At E4.5, the epiblast is a coherent ball of tightly packed apolar cells with uniform expression of E-cad on the cell membrane. As the blastocyst initiates implantation, a burst of cell proliferation rapidly increases the size of the embryo, and the growing ICM expands into the blastocoel cavity. Between E4.5 and E5.5, the epiblast exits the naïve pluripotent state and undergoes a process of epithelialization, resulting in the de novo establishment of apical-basal polarity. During this process, E-cad is removed from the newly specified apical domain, while the CD34 family of antiadhesins are delivered there. This generates a site of low intercellular adhesion in the center of the epiblast, where all apical membranes of the individual pluripotent cells cluster together. Water influx driven by the combined activity of Na<sup>+</sup>/K<sup>+</sup> and Cl<sup>–</sup> pumps builds pressure that opens up the apical membranes and initiates lumen formation. Water also enters the emerging proamniotic cavity during cell division, streaming between neighboring cells or following the cleavage furrow during cytokinesis. The source of water that fills up the proamniotic cavity is the blastocoel fluid, which encompasses the growing egg cylinder.

The formation of the proamniotic cavity transforms the epiblast from a simple ball of cells to a folded (cup-shaped) epithelial monolayer. The ultrastructural analysis of the pluripotent lineage showed uninterrupted cell-cell contacts tightly packing the epiblast cells of the E4.5 blastocyst. However, at E5.5, we found multiple intermembranous spaces even between cells that are not undergoing mitosis. This is reminiscent to the basolateral membrane fracking observed in epithelial sheets and morula stage embryos caused by an influx of pressurized fluid (16, 33). Thus, the microlumens in the postimplantation

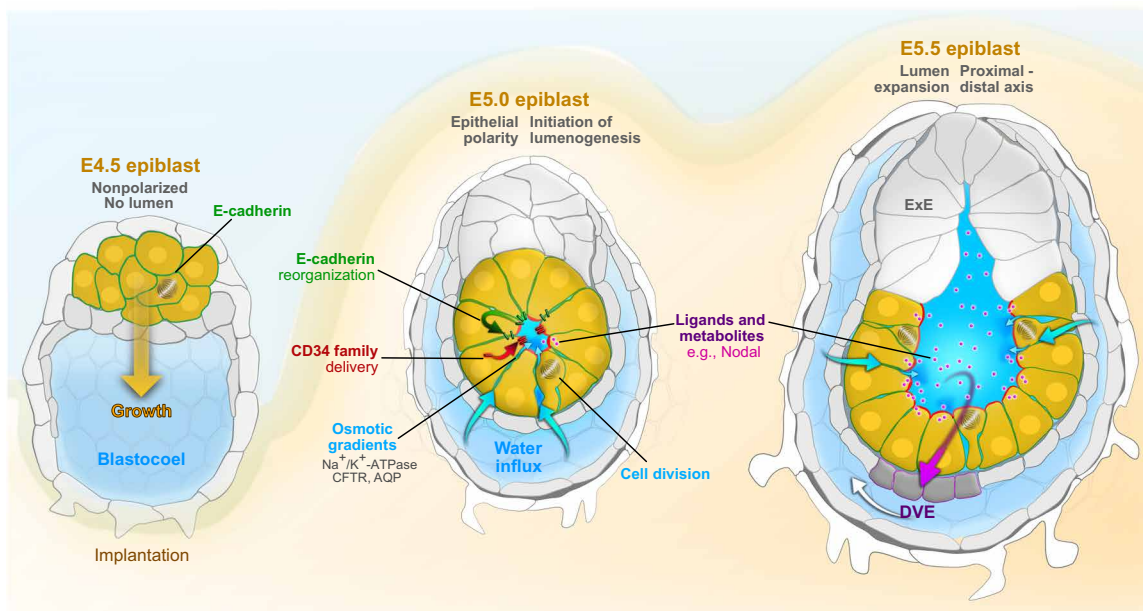


**Fig. 8. Formation and function of the proamniotic cavity.** Schematic representation of the proposed model of proamniotic cavity formation and function. AQP, Aquaporins.

epiblast could be generated as a result of hydraulic fracture locally interrupting E-cad-mediated cell-cell contacts. Accordingly, when E-cad adhesion was reinforced via streptavidin/biotin interaction, it was sufficient to block the formation of these intermembranous pockets.

The early postimplantation morphogenesis is associated with the establishment of signaling centers in the embryo (34). The DVE, which migrates to from the AVE, specifies the anterior part of the underlying epiblast (future head), and the primitive streak defines the posterior region (future tail); this process requires fine-tuned communication between the embryonic and the extraembryonic lineages (35). We found that the proamniotic cavity acts as a micro-environment for ligands and associated factors of critical developmental pathways, such as the Nodal signaling cascade. Accordingly, embryos in which the formation of the proamniotic cavity was experimentally blocked displayed features of impeded Nodal signaling, such as failure to properly induce signaling centers, failure to establish the early body axes, and developmental arrest before gastrulation. Ligands of other signaling pathways, as well as antagonists and metabolites, may also accumulate into the luminal fluid. These para- and autocrine signaling molecules may not only regulate stemness, differentiation, and patterning but also be involved in maintaining the general tissue homeostasis, including the processes of cell competition, proliferation, and apoptosis. Moreover, maternally provided factors such as members of the Activin family, immunoglobulins, and high-density lipoprotein can cross the Reichert's membrane and reach the developing embryo (36–39). Thus, the water influx from the blastocoel (the space between the parietal and visceral endoderm at E5.5) to the proamniotic cavity may enable the uptake of molecules from the maternal environment.

Beyond E5.5, the proamniotic cavity may also play a role as structural component that physically separates already established signaling centers. For instance, the AVE and the primitive streak, which are positioned on the opposite ends of the cup-shaped epiblast, also produce opposing signaling cues: The AVE expresses Nodal and Wnt antagonist, whereas the primitive streak exhibits high Nodal and Wnt activity (35). The close proximity of these centers may lead to a “tug of war” over the patterning of the epiblast; therefore, the in-between luminal space may provide the necessary spatial distance for adequate function without cross-interference.

In summary, we found that epiblast lumenogenesis is driven by the reorganization of intercellular adhesion, vectorial fluid transport, and mitotic paracellular water influx from the blastocoel. We determined that the proamniotic cavity is required for the intrinsic communication of the early lineages, enabling proper growth and patterning of the postimplantation embryo. These general principles of the generation and function of the proamniotic cavity are likely shared with the embryonic lumenogenesis in other mammalian species, including the formation of the amniotic cavity in human embryos.

## MATERIALS AND METHODS

### Cell lines

The ESCs were maintained on gelatine-coated plates in high-glucose Dulbecco's modified Eagle's medium (DMEM) supplemented with 15% fetal bovine serum (FBS), 2 mM L-glutamine, 1 mM sodium pyruvate, 1% (v/v) nonessential amino acids, penicillin-streptomycin (50 U/ml) (P4333, Sigma-Aldrich), 0.15 mM 2-mercaptoethanol, and 2i/Lif [0.4 μM PD0325901, 3 μM CHIR99021, and Lif (4 ng/ml)], at

37°C, 5% CO<sub>2</sub> atmosphere in air. Where indicated, ESCs were cultured in N2B27 medium consisting of DMEM/F12 and Neurobasal medium (1:1) supplemented with 0.5% (v/v) N2, 0.5% (v/v) B27 without vitamin A, 2 mM L-glutamine, penicillin-streptomycin (50 U/ml), and 0.05 mM 2-mercaptoethanol supplemented with 2i/Lif or Fgf2/Activin A/KSR [hFgf2 (12 ng/ml), hActivin A (20 ng/ml), and 1% (v/v) knockout serum replacement]. Stable cell lines for constitutive transgene expression were generated using PiggyBac (PB) transposon system (40). The transgenes were cloned into PB transposon vectors and cotransfected with transposase encoding plasmid (pIB1-PyCAG-PBase) using Lipopfectamine 2000 based on the manufacturer's instructions. After 24 hours of transfection, puromycin (1 μg/ml) or G418 (300 μg/ml) was added to the culture medium for 5 days to select for stably transfected clones.

### Mice

The mice used in this study were at the age from 6 weeks to 5 months. The animals were maintained under a 14-hour light/10-hour dark cycle with free access to food and water. Female mice were housed in groups of up to four per cage, and male stud mice were housed individually. Embryos for experiments were derived from CD1 and B6C3F1 strains. B6C3F1 strain was used for production of tetraploid morulae for aggregation, and foster mothers of the CD1 strain were used as recipients for embryo transfer experiments. Preimplantation embryos were isolated by flushing the oviduct and uterus using M2 medium, whereas the peri- and postimplantation embryos were manually dissected out. E5.5 embryos expressing membrane tdTomato were derived from the mT/mG strain (41). GFP-Nodal expressing embryos were generated following morula aggregation of B6C3F1 morulae and GFP-Nodal ESCs. At blastocyst stage, the mural TE was excised and the embryos were grown to egg cylinder stage, as previously described (42). All mouse experiments were performed in accordance to the guidelines of the German Animal Welfare and approved by the Landesamt für Natur, Umwelt und Verbraucherschutz Nordrhein-Westfalen, Deutschland (State Agency for Nature, Environment and Consumer Protection of North Rhine-Westphalia, Germany).

### Plasmids

E-cad-WT-GFP and E-cad-LP-GFP containing V5 tag in the ectodomain were gifts from V. Bennett (Duke University Medical Center, NY) (8). E-cad-WT-tdTomato was generated by replacing the GFP tag of the E-cad-WT-GFP plasmid with tdTomato. E-cad-Strep-LP-GFP plasmid was constructed by replacing the V5 tag in E-cad-LP-GFP with streptavidin (TSA) (a gift from T. Sano; Addgene plasmid #17327; <http://n2t.net/addgene:17327>; RRID (Research Resource Identifiers): Addgene\_17327) (43). E-cad-Bio-LP-tdTomato was generated by inserting biotinylation sequence GLNDIFEAQKIEWHE in the position of the V5 tag in the ectodomain of E-cad-LP-tdTom. The E-cad containing constructs were cloned into PB transposon vector (pIB10-PB-CAG-cHA-IRES-Puro). BirA-Cerulean was constructed from BirA-ER (a gift from A. Ting; Addgene plasmid #20856; <http://n2t.net/addgene:20856>; RRID: Addgene\_20856) (44) by removing the endoplasmic reticulum signal sequence and inserting Cerulean in the C terminus of BirA and cloned into pIB229-PB-CAG-cHA-IRES-Neo. Histone H2B-tdTomato was generated by replacing the GFP sequence of Histone H2B-GFP construct (a gift from A.-K. Hadjantonakis; Addgene plasmid # 32610; <http://n2t.net/addgene:32610>; RRID: Addgene\_32610) (45) with tdTomato sequence and cloned into pIB229-PB-CAG-cHA-IRES-Neo. PX459-2A-Venus and PX459-2A-Cerulean

plasmids were constructed by replacing the puromycin sequence in PX459 (a gift from F. Zhang; Addgene plasmid #62988; <http://n2t.net/addgene:62988>; RRID: Addgene 62988) (46) with Venus and Cerulean, respectively.

### CRISPR-Cas9-mediated gene knockout in ESCs

Guide RNAs (gRNAs) listed in table S1 were designed using an E-CRISP design tool ([www.e-crisp.org/E-CRISP/designcrisp.html](http://www.e-crisp.org/E-CRISP/designcrisp.html)) and cloned into PX459-2A-Venus or PX459-2A-Cerulean vectors. The gRNAs were designed to target upstream and downstream introns to delete the intermediate critical exons and simultaneously generate a stop codon. The gRNA-containing plasmids were transfected into E14 ESCs, and after 48 hours, Venus and Cerulean double-positive cells were collected using fluorescence-activated cell sorting (FACS). These cells were plated on a 10-cm plate and cultured for picking individual ESC colonies. Gene ablation was assessed by polymerase chain reaction (PCR) using primers listed in table S1 and further verified on a protein level using immunohistochemistry. See table S1 containing the list of oligos.

### 3D ESC culture

ESCs were dissociated using 0.25% trypsin-EDTA and pelleted by centrifugation. The cell pellet was washed once with phosphate-buffered saline (PBS) and repelleted. Residual PBS was removed and the pellet was resuspended in Matrigel (1200 cells per 1- $\mu$ l Matrigel). The cell suspension was then plated on an eight-well ibidi  $\mu$ -plate and placed in a cell culture incubator at 37°C, 5% CO<sub>2</sub> atmosphere in air for 5 min to solidify the Matrigel. Each well was filled with N2B27 medium supplemented with 2i/Lif or Fgf2/Activin A/KSR and cultured for 36 to 72 hours at 37°C, 5% CO<sub>2</sub> atmosphere in air.

### DNA extraction and PCR

ESCs were washed once with PBS and incubated with DNA lysis buffer [10 mM tris-HCl (pH 7.5), 10 mM EDTA, 0.5% (v/v) SDS, and 10 mM NaCl] and proteinase K (1 mg/ml) at 55°C overnight. DNA was precipitated using 75 mM NaCl in ethanol and washed twice with 70% (v/v) ethanol. PCR was prepared using a GoTaq green master mix, and primers are listed in table S1.

### RNA extraction from ESCs grown in 3D culture and reverse transcription-PCR

To isolate ESCs cultured in Matrigel, the Matrigel was incubated in a 1:2 (v/v) mixture of 0.25% trypsin-EDTA and Accutase for 20 min. The Matrigel was periodically broken into pieces by manual pipetting. Cells were pelleted by centrifugation, and the pellet was washed once with PBS. RNA extraction and complementary DNA (cDNA) synthesis were carried out using the RNeasy Mini Kit and the SuperScript III CellsDirect cDNA Synthesis Kit, respectively, following the manufacturer's instructions. Reverse transcription PCR was prepared using iTag SYBR Green Supermix. Gene expression was normalized to  $\beta$ -actin.

### Site-specific biotinylation and Western blot

To induce biotinylation in 3D culture, ESCs expressing the biotin-streptavidin adhesion system were incubated with culture medium supplemented with 50  $\mu$ M D-Biotin for 24 hours. As a negative control, cells were cultured in the absence of biotin. Site-specific biotinylation was visualized by Western blotting, as follows. The cells were scraped, pelleted by centrifugation, and lysed in ice-cold

radioimmunoprecipitation assay buffer containing 25 mM tris-HCl (pH 7.4), 150 mM NaCl, 1% (v/v) NP-40, 0.5% (w/v) sodium deoxycholate, 0.1% (v/v) SDS, 1 $\times$  protease inhibitor cocktail, and 0.5 mM phenylmethylsulfonyl fluoride. Cleared lysates were obtained by centrifugation. Protein concentration was measured using the BCA Protein Assay Kit based on the manufacturer's instructions. Twenty micrograms of the total protein was separated in SDS-polyacrylamide gel electrophoresis gel along with the Precision Plus Protein Kaleidoscope protein standard and were subsequently transferred onto a polyvinylidene difluoride membrane. Following the transfer, the membrane was blocked in 5% milk in tris-buffered saline (TBS)-0.2% Triton X for 1 hour, washed three times in TBS-0.05% Tween 20 (TBS-T) for 5 min, and probed with a streptavidin-horseradish peroxidase (HRP) antibody (1:30,000 dilution) in 3% (w/v) bovine serum albumin (BSA) in TBS-T for 45 min. The probed membrane was incubated with ECL Western Blotting Detection Reagent for signal detection.

For antibody reprobing, the membrane was incubated in the HRP quenching buffer [30% (w/v) sodium azide and 15% (v/v) hydrogen peroxide in water] and washed three times in PBS-0.05% Tween 20 (PBS-T). The membrane was blocked in 5% milk in PBS-T for 1 hour and probed with primary antibodies overnight at 4°C with agitation. On the next day, the membrane was washed three times in PBS-T and incubated with secondary antibodies conjugated to HRP for 2 hours in room temperature. Chemiluminescence signal was detected using either ECL Western Blotting Detection Reagent or ECL Prime Western Blotting Detection Reagent.

To induce biotinylation *in vivo* in embryos generated following tetraploid complementation, foster mothers were injected intraperitoneally every day with 40 mg/kg body weight of D-biotin diluted in PBS from the day of the vaginal plug.

### Fluorescence-activated cell sorting

Cells were dissociated using 0.25% trypsin-EDTA and pelleted by centrifugation, and after that, the pellet was resuspended in 3% (v/v) FBS in PBS. FACSaria IIu Sorter (BD Biosciences) was used to select for live cells based on FSC (Forward Scatter) and SSC (Side Scatter) gating, followed by sorting cells positive for the fluorescent probe of interest.

### Decidua tissue clearing and immunofluorescence

E4.75 and E5.5 deciduae containing intact embryos were fixed in 4% PFA (Paraformaldehyde) for 1 hour, washed three times in 0.2% (v/v) Triton X in PBS, and permeabilized in 0.2% (v/v) Triton X and 20% (v/v) dimethyl sulfoxide (DMSO) in PBS overnight. For the next sequential steps of staining, the samples were kept on a rotatory shaker. The samples were incubated sequentially overnight in buffer A [0.1% (v/v) Tween 20, 0.1% (v/v) Triton X, 0.1% (w/v) sodium deoxycholate, 0.1% (v/v) NP-40, and 20% (v/v) DMSO in PBS], buffer B [0.2% (v/v) Triton X, 20% (v/v) DMSO, and 0.3 M glycine in PBS], and buffer C [0.2% (v/v) Triton X, 10% (v/v) DMSO, and 6% (v/v) donkey serum in PBS]. The samples were then incubated with primary antibodies diluted in primary antibody buffer [0.2% (v/v) Tween 20, heparin (10  $\mu$ g/ml), 5% (v/v) DMSO, and 3% (v/v) donkey serum in PBS] for 3 days, washed overnight in 0.2% (v/v) Triton X in PBS, and incubated with secondary antibodies and 4',6-diamidino-2-phenylindole (DAPI) diluted in secondary antibody buffer [0.2% (v/v) Tween 20, heparin (10  $\mu$ g/ml), and 3% (v/v) donkey serum in PBS], after an additional overnight wash in 0.2% (v/v) Triton X in PBS and subsequent two washes in PBS. For tissue clearing, the samples were

dehydrated sequentially in 50% (v/v) methanol, 70% (v/v) methanol, 95% (v/v) methanol, 100% (v/v) anhydrous methanol, and 100% (v/v) methanol for 1 hour each. Residual methanol was carefully removed from the samples. The deciduae were tissue-cleared using clearing solution [100% anhydrous methanol mixed with 1:2 (v/v) benzyl alcohol and benzyl benzoate (BABB solution) in a 1:1 ratio] for 4 hours. The samples were kept in the BABB solution for an additional 4 hours and then transferred into fresh BABB solution before imaging. See table S2 containing the list of antibodies.

### Immunofluorescence labeling and microscopy

Cells cultured into eight-well ibidi  $\mu$ -plates were fixed in 4% PFA for 20 min, washed twice in PBS, and permeabilized using 0.3% (v/v) Triton X in PBS for 15 min. After two washes in PBS, the cells were incubated in blocking buffer [3% (w/v) BSA in PBS] for 1 hour and subsequently incubated overnight at 4°C with primary antibodies diluted in the blocking buffer. On the next day, the sample was washed three times in PBS and incubated overnight at 4°C with secondary antibodies and DAPI diluted in the blocking buffer. After three washes in PBS, the samples were imaged or stored in PBS.

E3.5–E4.75 blastocysts were fixed in 4% PFA for 20 min and washed twice in wash buffer [1% (v/v) fetal calf serum in PBS]. The fixed embryos were permeabilized using 0.1 M glycine/0.3% (v/v) Triton X in PBS (5 min for E3.5–E4.5 embryos, 7 min for E4.75–E5.0 embryos, and 10 min for E5.5–E6.5 embryos) and washed twice. The embryos were then incubated with primary antibodies in blocking buffer [2% (v/v) FBS in PBS] overnight at 4°C. After two washes in the wash buffer, the embryos were incubated with secondary antibodies and DAPI in the blocking buffer, followed by two subsequent washes on the next day. Last, the embryos were mounted in droplets of wash buffer on 35-mm  $\mu$ -Dish glass-bottom plates, covered with mineral oil, and imaged.

Postimplantation embryos (E5.0–E6.5) were fixed, permeabilized, and stained according to the decidua staining protocol without the tissue-clearing step. Images were acquired on Leica SP5, Leica SP8 (Leica Microsystems), or Zeiss LSM780 confocal microscope systems. See table S2 containing the list of antibodies.

### Time-lapse microscopy

Time-lapse imaging was performed using a Dragonfly spinning disc confocal microscope (Oxford instruments). Where indicated, LY and live-cell DNA staining dye (Sir-DNA) were included in the culture medium. Reichert's membrane-free E5.5 embryos were placed in M2 medium during imaging. All samples were imaged in a humidified chamber at 37°C, 5% CO<sub>2</sub> atmosphere in air.

### Electron microscopy

The samples were initially fixed by adding 2× concentrated fixative, 4% glutaraldehyde and 4% paraformaldehyde, in 0.1 M cacodylate buffer (pH 7.2) to the culture medium. After 10 min, the solution was replaced by 1× concentrated fixative, 2% glutaraldehyde and 2% paraformaldehyde, in 0.1 M cacodylate buffer (pH 7.2) and further fixed for 2 hours at room temperature.

For transmission electron microscopy, the specimen was cut into small cubes (about 1 mm<sup>3</sup>) and postfixed in 1% osmium tetroxide containing 1.5% potassium ferrocyanide. The cubes were incubated in 0.5% uranylacetate in 70% ethanol at 4°C overnight. Subsequently, the specimen was further dehydrated in ethanol with a final wash in propyleneoxide, which is required to remove last remnants of water

from the Matrigel. The sample was then infiltrated with epon, which was polymerized at 60°C. Sixty-nanometer ultrathin sections were cut on an ultramicrotome (UC6, Leica, Austria) and collected on filmed 50-mesh copper grids and counterstained with lead citrate. The sections were analyzed at 80 kV on a Tecnai 12-biotwin (Thermo Fisher Scientific, Eindhoven, The Netherlands). Images of representative areas were acquired on a 2K charge-coupled device camera (Veleta, EMSIS, MPI-MB).

For serial block-face scanning electron microscopy, the primary fixed samples needed a higher contrast staining, according to a previously published protocol (47). Sequential treatment of osmium tetroxide and thiocarbohydrazide (OTOTO) was used to increase the specimen contrast. Preselected samples were provided to L. Hekking (Thermo Fisher Scientific, NanoPort, Eindhoven, The Netherlands) for further analysis using Volumescape. A resin block of 1 mm by 1.5 mm was mounted on a Volumescape stub (Agar Scientific, USA) and immobilized using a two-component silver epoxy glue (Ted Pella, USA). After curing of the silver epoxy, the resin block was further trimmed down to approximately 1 mm by 550  $\mu$ m by 200  $\mu$ m, thereby taking care to keep the sample in the middle of the block. The sample was then sputter-coated with a layer of platinum and the top surface was exposed by a diamond knife. The serial images were collected using a serial block-face imaging scanning electron microscope that was equipped with an in-chamber microtome (Volumescape, Thermo Fisher Scientific). Four hundred fifty images were acquired using backscatter electrons at 1.8 keV in high-vacuum conditions. Four different regions of interest were acquired every 40 nm with a pixel size of 12 nm per pixel. The data were aligned, processed, and segmented using visualization software (Amira, Thermo Fisher Scientific).

### Image analysis

All light microscopy data were processed and analyzed using Fiji software (<http://fiji.sc>) (48). Quantification of lumen volume of ESCs cultured in 3D was done using Measure Stack plugin ([www.optinav.info/imagej.html](http://www.optinav.info/imagej.html)).

### Statistical analysis

Statistical analysis was performed using GraphPad Prism. Values are presented as means  $\pm$  SEM. Statistical significance was calculated using a two-tailed Student's *t* test (two groups) or analysis of variance (ANOVA) (multiple groups) with a Tukey's post hoc test.

### SUPPLEMENTARY MATERIALS

Supplementary material for this article is available at <http://advances.sciencemag.org/cgi/content/full/7/11/eabe1640/DC1>

[View/request a protocol for this paper from Bio-protocol.](#)

### REFERENCES AND NOTES

1. N. Govindasamy, B. Duethorn, H. O. Oezgueldez, Y. S. Kim, I. Bedzhov, Test-tube embryos - mouse and human development in vitro to blastocyst stage and beyond. *Int. J. Dev. Biol.* **63**, 203–215 (2019).
2. I. Bedzhov, M. Zernicka-Goetz, Self-organizing properties of mouse pluripotent cells initiate morphogenesis upon implantation. *Cell* **156**, 1032–1044 (2014).
3. R. Fan, Y. S. Kim, J. Wu, R. Chen, D. Zeuschner, K. Mildner, K. Adachi, G. Wu, S. Galatidou, J. Li, H. R. Schöler, S. A. Leidel, I. Bedzhov, Wnt/Beta-catenin/Esrrb signalling controls the tissue-scale reorganization and maintenance of the pluripotent lineage during murine embryonic diapause. *Nat. Commun.* **11**, 5499 (2020).
4. E. Coucouvanis, G. R. Martin, Signals for death and survival: A two-step mechanism for cavitation in the vertebrate embryo. *Cell* **83**, 279–287 (1995).
5. L. Wolpert, *Principles of Development* (Oxford University Press, 2011).

6. M. Kinoshita, A. Smith, Pluripotency deconstructed. *Dev. Growth Differ.* **60**, 44–52 (2018).
7. K. Hayashi, H. Ohta, K. Kurimoto, S. Aramaki, M. Saitou, Reconstitution of the mouse germ cell specification pathway in culture by pluripotent stem cells. *Cell* **146**, 519–532 (2011).
8. P. M. Jenkins, C. Vasavda, J. Hostettler, J. Q. Davis, K. Abdi, V. Bennett, E-cadherin polarity is determined by a multifunction motif mediating lateral membrane retention through ankyrin-G and apical-lateral transcytosis through clathrin. *J. Biol. Chem.* **288**, 14018–14031 (2013).
9. T. Hara, Y. Nakano, M. Tanaka, K. Tamura, T. Sekiguchi, K. Minehata, N. G. Copeland, N. A. Jenkins, M. Okabe, H. Kogo, Y. Mukoyama, A. Miyajima, Identification of podocalyxin-like protein 1 as a novel cell surface marker for hemangioblasts in the murine aorta-gonad-mesonephros region. *Immunity* **11**, 567–578 (1999).
10. D. Meder, A. Shevchenko, K. Simons, J. Füllekrug, Gp135/podocalyxin and NHERF-2 participate in the formation of a preapical domain during polarization of MDCK cells. *J. Cell Biol.* **168**, 303–313 (2005).
11. R. A. Orlando, T. Takeda, B. Zak, S. Schmieder, V. M. Benoist, T. McQuistan, H. Furthmayr, M. G. Farquhar, The glomerular epithelial cell anti-adhesion podocalyxin associates with the actin cytoskeleton through interactions with ezrin. *J. Am. Soc. Nephrol.* **12**, 1589–1598 (2001).
12. M. N. Shahbazi, A. Scialdone, N. Skorupska, A. Weberling, G. Recher, M. Zhu, A. Jedrusik, L. G. Devito, L. Noli, I. C. Macaulay, C. Buecker, Y. Khalaf, D. Illic, T. Voet, J. C. Marioni, M. Zernicka-Goetz, Pluripotent state transitions coordinate morphogenesis in mouse and human embryos. *Nature* **552**, 239–243 (2017).
13. J. Cheng, S. Baumhueter, G. Cacalano, K. Carver-Moore, H. Thibodeaux, R. Thomas, H. E. Broxmeyer, S. Cooper, N. Hague, M. Moore, L. A. Lasky, Hematopoietic defects in mice lacking the sialomucin CD34. *Blood* **87**, 479–490 (1996).
14. R. Doyonnas, D. B. Kershaw, C. Duhme, H. Merckens, S. Chelliah, T. Graf, K. M. McNagny, Anuria, omphalocele, and perinatal lethality in mice lacking the CD34-related protein podocalyxin. *J. Exp. Med.* **194**, 13–28 (2001).
15. Z. Yang, S. E. Zimmerman, J. Tsunozumi, C. Braitsch, C. Trent, D. M. Bryant, O. Cleaver, C. González-Manchón, D. K. Marciano, Role of CD34 family members in lumen formation in the developing kidney. *Dev. Biol.* **418**, 66–74 (2016).
16. J. G. Dumortier, M. Le Verge-Serandour, A. F. Tortorelli, A. Mielke, L. de Plater, H. Turlier, J.-L. Maître, Hydraulic fracturing and active coarsening position the lumen of the mouse blastocyst. *Science* **365**, 465–468 (2019).
17. A. Q. Ryan, C. J. Chan, F. Graner, T. Hiiragi, Lumen expansion facilitates epiblast-primitive endoderm fate specification during mouse blastocyst formation. *Dev. Cell* **51**, 684–697.e4 (2019).
18. R. Scognamiglio, N. Cabezas-Wallscheid, M. C. Thier, S. Altamura, A. Reyes, Á. M. Prendergast, D. Baumgärtner, L. S. Carnevalli, A. Atzberger, S. Haas, L. von Paleske, T. Boroviak, P. Wörsdörfer, M. A. G. Essers, U. Klotz, R. N. Eisenman, F. Edenhofer, P. Bertone, W. Huber, F. van der Hoeven, A. Smith, A. Trumpp, Myc depletion induces a pluripotent dormant state mimicking diapause. *Cell* **164**, 668–680 (2016).
19. F. L. Conlon, K. M. Lyons, N. Takasau, K. S. Barth, A. Kispert, B. Herrmann, E. J. Robertson, A primary requirement for nodal in the formation and maintenance of the primitive streak in the mouse. *Development* **120**, 1919–1928 (1994).
20. Z. Gu, M. Nomura, B. B. Simpson, H. Lei, A. Feijen, J. van den Eijnden-van Raaij, P. K. Donahoe, E. Li, The type I activin receptor ActRIB is required for egg cylinder organization and gastrulation in the mouse. *Gene Dev.* **12**, 844–857 (1998).
21. M. M. Shen, Nodal signaling: Developmental roles and regulation. *Development* **134**, 1023–1034 (2007).
22. J. Song, S. P. Oh, H. Schrewe, M. Nomura, H. Lei, M. Okano, T. Gridley, E. Li, The type II activin receptors are essential for egg cylinder growth, gastrulation, and rostral head development in mice. *Dev. Biol.* **213**, 157–169 (1999).
23. M. Weinstein, X. Yang, C. Li, X. Xu, J. Gotay, C.-X. Deng, Failure of egg cylinder elongation and mesoderm induction in mouse embryos lacking the tumor suppressor *smad2*. *Proc. Natl. Acad. Sci. U.S.A.* **95**, 9378–9383 (1998).
24. E. J. Robertson, D. P. Norris, J. Brennan, E. K. Bikoff, Control of early anterior-posterior patterning in the mouse embryo by TGF- $\beta$  signalling. *Philos. Trans. R. Soc. Lond. B Biol. Sci.* **358**, 1351–1357 (2003).
25. D. Mesnard, M. Donnison, C. Fuerer, P. L. Pfeffer, D. B. Constam, The microenvironment patterns the pluripotent mouse epiblast through paracrine Furin and Pace4 proteolytic activities. *Genes Dev.* **25**, 1871–1880 (2011).
26. M. Yamamoto, H. Beppu, K. Takaoka, C. Meno, E. Li, K. Miyazono, H. Hamada, Antagonism between Smad1 and Smad2 signaling determines the site of distal visceral endoderm formation in the mouse embryo. *J. Cell Biol.* **184**, 323–334 (2009).
27. C. Chen, S. M. Ware, A. Sato, D. E. Houston-Hawkins, R. Habas, M. M. Matzuk, M. M. Shen, C. W. Brown, The Vg1-related protein Gdf3 acts in a Nodal signaling pathway in the pre-gastrulation mouse embryo. *Development* **133**, 319–329 (2006).
28. O. Andersson, P. Bertolino, C. F. Ibáñez, Distinct and cooperative roles of mammalian Vg1 homologs GDF1 and GDF3 during early embryonic development. *Dev. Biol.* **311**, 500–511 (2007).
29. D. Mesnard, M. Guzman-Ayala, D. B. Constam, Nodal specifies embryonic visceral endoderm and sustains pluripotent cells in the epiblast before overt axial patterning. *Development* **133**, 2497–2505 (2006).
30. J. Brennan, C. C. Lu, D. P. Norris, T. A. Rodriguez, R. S. P. Beddington, E. J. Robertson, Nodal signalling in the epiblast patterns the early mouse embryo. *Nature* **411**, 965–969 (2001).
31. A. D. Senft, I. Costello, H. W. King, A. W. Mould, E. K. Bikoff, E. J. Robertson, Combinatorial Smad2/3 activities downstream of nodal signaling maintain embryonic/extra-embryonic cell identities during lineage priming. *Cell Rep.* **24**, 1977–1985.e7 (2018).
32. A. D. Senft, E. K. Bikoff, E. J. Robertson, I. Costello, Genetic dissection of Nodal and Bmp signalling requirements during primordial germ cell development in mouse. *Nat. Commun.* **10**, 1089 (2019).
33. L. Casares, R. Vincent, D. Zalvidea, N. Campillo, D. Navajas, M. Arroyo, X. Trepau, Hydraulic fracture during epithelial stretching. *Nat. Mater.* **14**, 343–351 (2015).
34. I. Bedzhov, M. Bialecka, A. Zielinska, J. Kosalka, F. Antonica, A. J. Thompson, K. Franze, M. Zernicka-Goetz, Development of the anterior-posterior axis is a self-organizing process in the absence of maternal cues in the mouse embryo. *Cell Res.* **25**, 1368–1371 (2015).
35. K. Takaoka, H. Hamada, Cell fate decisions and axis determination in the early mouse embryo. *Development* **139**, 3–14 (2012).
36. R. L. Jones, T. J. Kaitu'u-Lino, G. Nie, L. G. Sanchez-Partida, J. K. Findlay, L. A. Salamonsen, Complex expression patterns support potential roles for maternally derived activins in the establishment of pregnancy in mouse. *Reproduction* **132**, 799–810 (2006).
37. R. M. Albano, R. Arkell, R. S. Beddington, J. C. Smith, Expression of inhibin subunits and follistatin during postimplantation mouse development: Decidual expression of activin and expression of follistatin in primitive streak, somites and hindbrain. *Development* **120**, 803–813 (1994).
38. O. Bernard, M. A. Ripoché, D. Bennett, Distribution of maternal immunoglobulins in the mouse uterus and embryo in the days after implantation. *J. Exp. Med.* **145**, 58–75 (1977).
39. B. T. Smith, J. C. Mussell, P. A. Fleming, J. L. Barth, D. D. Spyropoulos, M. A. Cooley, C. J. Drake, W. S. Argraves, Targeted disruption of cubilin reveals essential developmental roles in the structure and function of endoderm and in somite formation. *BMC Dev. Biol.* **6**, 30 (2006).
40. W. Wang, C. Lin, D. Lu, Z. Ning, T. Cox, D. Melvin, X. Wang, A. Bradley, P. Liu, Chromosomal transposition of *PiggyBac* in mouse embryonic stem cells. *Proc. Natl. Acad. Sci. U.S.A.* **105**, 9290–9295 (2008).
41. M. D. Muzumdar, B. Tasic, K. Miyamichi, L. Li, L. Luo, A global double-fluorescent Cre reporter mouse. *Genesis* **45**, 593–605 (2007).
42. N. Govindasamy, I. Bedzhov, Isolation and culture of periimplantation and early postimplantation mouse embryos. *Methods Mol. Biol.* **2006**, 373–382 (2019).
43. T. Sano, M. W. Pandori, X. M. Chen, C. L. Smith, C. R. Cantor, Recombinant core streptavidins. A minimum-sized core streptavidin has enhanced structural stability and higher accessibility to biotinylated macromolecules. *J. Biol. Chem.* **270**, 28204–28209 (1995).
44. M. Howarth, W. Liu, S. Puthenveetil, Y. Zheng, L. F. Marshall, M. M. Schmidt, K. D. Wittrup, M. G. Bawendi, A. Y. Ting, Monovalent, reduced-size quantum dots for imaging receptors on living cells. *Nat. Methods* **5**, 397–399 (2008).
45. A. Ferrer-Vaquer, A. Piliszek, G. Tian, R. J. Aho, D. Dufort, A.-K. Hadjantonakis, A sensitive and bright single-cell resolution live imaging reporter of Wnt/ $\beta$ -catenin signaling in the mouse. *BMC Dev. Biol.* **10**, 121 (2010).
46. F. A. Ran, P. D. Hsu, J. Wright, V. Agarwala, D. A. Scott, F. Zhang, Genome engineering using the CRISPR-Cas9 system. *Nat. Protoc.* **8**, 2281–2308 (2013).
47. T. J. Deerincq, E. A. Bushong, A. Thor, M. H. Ellisman, NCMIR methods for 3D EM: A new protocol for preparation of biological specimens for serial block face scanning electron microscopy. *Nat. Center Microsc. Imag. Res.*, 6–8 (2010).
48. J. Schindelin, I. Arganda-Carreras, E. Frise, V. Kaynig, M. Longair, T. Pietzsch, S. Preibisch, C. Rueden, S. Saalfeld, B. Schmid, J.-Y. Tinevez, D. J. White, V. Hartenstein, K. Eliceiri, P. Tomancak, A. Cardona, Fiji: An open-source platform for biological-image analysis. *Nat. Methods* **9**, 676–682 (2012).

**Acknowledgments:** We thank V. Bennett for providing the E-cad-WT-GFP and E-cad-LP-GFP plasmids; N. Govindasamy for developing the decidua tissue-clearing protocol; H.-W. Choi for providing E14 ESCs; H. R. Schöler and R. H. Adams for providing access to key infrastructure, equipment, and reagents; B. Trappmann for providing access to the Dragonfly microscope; H. Brinkmann for the general technical assistance; R. Wedlich-Söldner and A. Püschel, as well as all laboratory members, for constructive discussions and suggestions; D. B. Constam for providing the Nodal ko ESCs and for the constructive discussions; and C. Brenneka for proofreading the manuscript. **Funding:** This work was supported by the German Research Foundation (DFG) Emmy Noether grant (BE 5800/1-1) to I.B. and CIM Pilot project grant (PP-2016-16) to Y.S.K.; Y.S.K. is supported by the International Max Planck Research School, Molecular Biomedicine, Münster, Germany. **Author contributions:** I.B. and Y.S.K. conceived the study, designed experiments, and interpreted the results. I.B. and Y.S.K. wrote the

manuscript. I.B. and R.F. performed embryo micromanipulations. L.K. and N.K.-R. performed the tetraploid complementation and embryo transfer experiments. D.Z. and K.M. performed the transmission electron microscopy. L.H. performed the serial block-face scanning electron microscopy. M.S. performed FACS analysis. **Competing interests:** The authors declare that they have no competing interests. **Data and materials availability:** All data needed to evaluate the conclusions in the paper are present in the paper and/or the Supplementary Materials. Further information and requests for resources and reagents should be directed to the corresponding author I.B. (ivan.bedzhov@mpi-muenster.mpg.de).

Submitted 4 August 2020

Accepted 26 January 2021

Published 10 March 2021

10.1126/sciadv.abe1640

**Citation:** Y. S. Kim, R. Fan, L. Kremer, N. Kuempel-Rink, K. Mildner, D. Zeuschner, L. Hekking, M. Stehling, I. Bedzhov, Deciphering epiblast lumenogenesis reveals proamniotic cavity control of embryo growth and patterning. *Sci. Adv.* **7**, eabe1640 (2021).